

The rapidly advancing contact line Part-1: Navier slip and microscale inertial effects

Yash Kulkarni[†]¹, Tomas Fullana¹, Stéphane Popinet¹ and Stéphane Zaleski[†]^{1,2}

¹Sorbonne Université and CNRS, UMR 7190, Institut Jean le Rond d'Alembert, F75005 Paris, France

²Institut Universitaire de France, UMR 7190, Institut Jean le Rond d'Alembert, F75005 Paris, France

(Received xx; revised xx; accepted xx)

Curtain coating, in which a moving plate is coated by a falling liquid sheet, sustains rapidly advancing contact lines at large capillary numbers $Ca \sim \mathcal{O}(1)$, based on the plate speed. Steady-state solutions exist up to a critical capillary number, beyond which wetting failure occurs through the entrainment of air bubbles. In the steady regime, experiments report an acceleration of the velocity along the fluid-fluid interface as the contact line is approached, down to a few tens of micrometres, and this observation has been interpreted as evidence against the Navier slip model. A central question is whether this observed acceleration is compatible with slip models. Here we show that it is. Although the Navier slip model implies a vanishing velocity at the contact line, the experimentally accessible microscale region (outer region) lies outside the slip region. This is precisely what makes the curtain coating setup revealing as the local Reynolds number, based on the distance from the contact line $r \sim 10 \mu\text{m}$, is order unity and the flow is therefore governed by local inertial effects. Our two-phase Navier-Stokes Volume-of-Fluid simulations with quadtree adaptive mesh refinement allow us to resolve the smallest scales and investigate the flow subject to a Navier slip boundary condition and a fixed contact angle. The simulations reproduce the non-monotonic dependence of the critical capillary number on global Reynolds number, based on the feed-flow velocity, as well as the variation of the macroscopic contact angle at the inflection point, in agreement with the predictions of Liu *et al.* (2016). Moreover, the interfacial velocity in the microscale region is well described by an inertially corrected wedge flow solution whose wedge angle is set by its value at the inflection point, with agreement improving as the slip length is reduced; at larger scales the interface bending follows the Benney & Timson (1980) solution. These inertial effects, absent from a pure Stokes description, are essential to the description of the flow in the experimentally observable region, and qualitative observations at the microscale region therefore do not provide a decisive invalidation of slip models for rapidly advancing contact lines.

Key words: contact lines, Navier slip, inertial effects

[†] Email address for correspondence: yash.kulkarni@dalembert.upmc.fr

[‡] Email address for correspondence: stephane.zaleski@sorbonne-universite.fr

1. Introduction

A three-phase contact line is the line where a fluid–fluid interface meets a solid surface. The static equilibrium contact line is understood thermodynamically through the Young relation, which has been known for more than two centuries (Young 1805). The dynamics of a moving contact line, however, have remained controversial for decades (Hocking 1992; Blake & Shikhmurzaev 2002; Eggers & Evans 2004; Shikhmurzaev 2006). In this paper, we examine the widely used Navier-slip boundary condition in the curtain-coating configuration, restricting attention to steady two-phase motion in the continuum sharp-interface limit.

Theories of the contact line can be distinguished as to whether they predict the contact angle as a boundary condition for a continuously differentiable interface, or whether the contact angle is defined at some defined scale, as an angle at some distance l_M . In the second case to make the contact angle observable by optical methods one must specify $l_M \simeq 1\mu\text{m}$ or larger. It is clear that the first option leads to a description of the problem *ab initio* while the second description must be inferred from a fundamental theory. We typically call the first angle the nanoscopic contact angle θ_n while the angle at the scale l_M can be called the apparent contact angle θ_M . While the apparent angle may be a function of non-local properties of the flow, such as entry flow conditions far from the contact line (see Blake *et al.* (1999) for an example), the nanoscopic angle is most often assumed to be a “local” function of the flow properties. What local means here is sometimes difficult to express precisely, so giving some specific formulations is preferable. The simplest assumption is a fixed nanoscopic dynamic angle equal to the equilibrium angle

$$\theta_n = \theta_e. \quad (1.1)$$

Based on kinetic theory considerations and molecular dynamics a more general formulation is obtained (Blake & Haynes 1969; Qian *et al.* 2006) as

$$U_{CL} = f(\theta_n), \quad (1.2)$$

where the function f depends on the three materials being used. In addition for given materials a dependency on local temperature, pressure and electromagnetic field could appear. The mobility relation (1.2) needs to be associated with a boundary condition for the fluid momentum equations. For a moving fluid interface, the traditional no-slip boundary condition was shown to have a force singularity at the contact line by Huh & Scriven (1971) suggesting that the contact line motion is impossible. This was analysed from a Lagrangian point of view by Dussan V. & Davis (1974) who showed that under the assumption of the experimentally observed rolling motion for the fluid-fluid interface along with the no-slip boundary condition, the velocity of the contact line is multi-valued. A suggested remedy was to allow a small slip velocity at the fluid-solid interface (Dussan V. 1976), quantified by the slip length. A simple example is

$$u + \lambda \frac{\partial u}{\partial y} = U_S. \quad (1.3)$$

Here u represents the tangential component (along the solid substrate) of the fluid velocity at the fluid-solid interface (no-penetration condition sets the normal component $v = 0$ at the solid) and U_S represents the velocity of the solid substrate, both are in the laboratory frame of reference. λ is the slip length, typically of the order of nanometers. This is known as the Navier (1823) slip boundary condition (NBC).

For steady-state contact line motion in the Stokes limit, it was shown by Hocking

(1977) that the NBC (constant slip length) removes the force singularity and a finite expression for the wall shear stress, assuming a flat interface was also obtained. The velocity u at the contact line is also related to the contact line velocity by

$$U_{CL} = u(x_{CL}) - U_S, \quad (1.4)$$

where x_{CL} is the contact line position. A more general class of mobility relation can occur if the local properties of the flow field are taken into account. For example, the Generalized Navier Boundary Condition for a sharp interface method (Qian *et al.* 2006) reads

$$U_{CL} - \lambda \partial_y u = \frac{\sigma}{\mu} [\cos(\theta) - \cos(\theta_s)] g\left(\frac{x}{\epsilon}\right), \quad (1.5)$$

where θ_s is the static contact angle, μ the liquid viscosity, g a smoothed δ function and ϵ a microscopic length. Assuming a C^1 velocity field up to the contact line, the normal vector at the interface (and hence the contact angle) rotates as the contact line moves (Fricke *et al.* 2019), resulting in $\partial_y u = -\dot{\theta}$ and yielding the generalized mobility law

$$U_{CL} = f(\theta, \dot{\theta}) = f(\theta, -\partial_y u). \quad (1.6)$$

Such a law is still local, albeit more general than the elementary mobility law (1.2). Even more general laws may be found in the form

$$U_{CL} = f(\theta, \dot{\theta}, \chi_1, \chi_2) \quad (1.7)$$

where χ_1, χ_2 are some local properties of the flow, such as derivatives of the velocity field or of the interface height. For example, the super slip condition involves $\partial_{yy}^2 u$ (Kulkarni *et al.* 2023). Many other boundary conditions have been suggested (Bonn *et al.* 2009) sometimes involving additional physical effects (intermolecular forces, tensio-active materials, interface roughness, non-constant surface tension Shikhmurzaev (1993)). Almost of all of these theories involve very small length scales and are thus extremely difficult to verify experimentally. Moreover it is well known (Cox 1986; Voinov 1976) that large curvatures $1/R$ appear near the contact line, so that the angle predicted at the nanometer scale may be very different from the angle observable by optical methods at the micrometer scale. As a result theories of the contact line boundary condition such as the NBC may only be tested indirectly, solving the Navier-Stokes equations over the whole range of scales from below the nanoscopic scales λ or R to the outer flow scales. The problem becomes especially challenging when the contact line advances rapidly. In curtain coating, steady solutions with $Ca = O(1)$ are possible, so the contact-line speed can be large enough for the local Reynolds number based on the distance from the contact line to become order unity already at experimentally accessible micrometric scales. In that regime, a purely Stokes-flow description is no longer sufficient in the observable region, so asymptotic theories based on creeping-flow assumptions, such as those of Cox (1986); Voinov (1976), do not directly apply there. Since the interface can bend substantially between the experimentally resolved micrometric scale and the nanometric scale at which a microscopic contact-line model is postulated, resolving the full multiscale structure becomes a formidable challenge. As far as the authors know the only works that cover the full range of scales from the nanoscopic to the centimetre scale are those of Wilson *et al.* (2006) in the curtain-coating setup and Kamal *et al.* (2019) in the cusp setup. Both of these works assumed a free surface. While Wilson *et al.* (2006) solve the full Navier-Stokes, Chan *et al.* (2020) solve the stokes flow only. This paper aims to do a full-range computation with the two-phase Navier-Stokes equations. However, it turns out that a simulation that starts with a grid size that accurately resolves the nanometer scale, and hence is markedly smaller than the nanometer, and reaches the

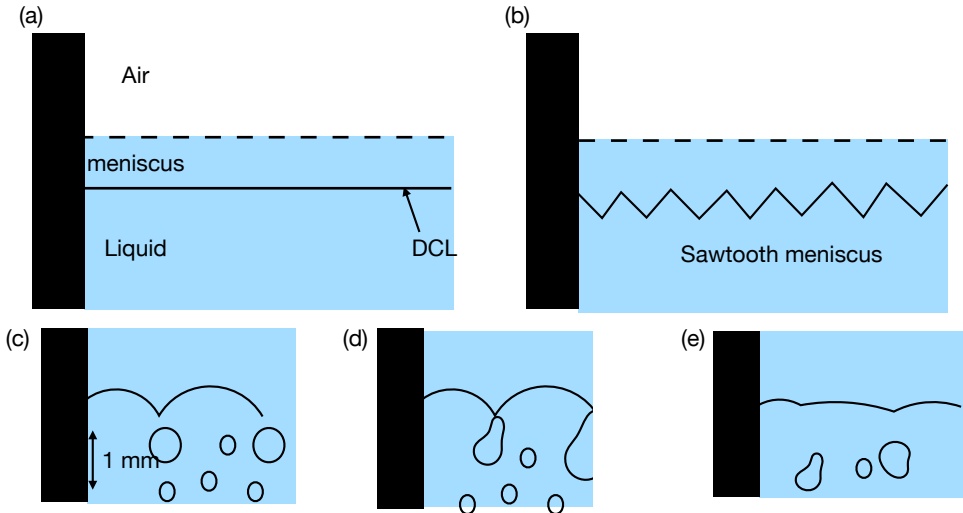


Figure 1: Schematic representation of air entrainment and wetting failure, based on the experimental sequence shown in Fig. 4 of Vandre *et al.* (2014). (a) Stable steady-state condition. (b) Onset of wetting failure, marked by the appearance of a sawtooth meniscus. (c) Entrainment of an air film. (d) Rupture of the air film and bubble formation. (e) Bubbles and residual air films left on the coated substrate.

scale of several centimeters is out of reach with current Volume-Of-Fluid methods or any other two-phase direct numerical simulation methods. This paper thus explores a very wide, but not the full range of scales of a typical experiment, going down only to slip lengths of a hundred nanometers.

1.1. The curtain coating setup

The problem we investigate numerically in this paper is curtain coating, which is a dynamic wetting setup. In such setups, a liquid displaces a gas (usually ambient air) on a flat solid substrate or in other words, coats the solid substrate. The dynamic wetting phenomenon has wide industrial applications as it forms the basis of many coating processes. It is known that beyond a critical substrate speed, wetting failure occurs, which is marked by air entrainment in the form of thin films and bubbles. Figure 1, taken from the experiments of Vandre *et al.* (2014), shows the onset of wetting failure for the plunging plate setup. Such entrained bubbles and films degrade the quality of the coated product and are often undesirable (Weinstein & Ruschak 2004). Thus, one would like to delay wetting failure as much as possible in industrial applications. The *hydrodynamic assist* effect below indeed speeds up to the order of meters per second (Blake *et al.* 1999).

The schematic of the curtain coating setup is shown in figure 2. The liquid is falling from the top with a feed flow velocity V , the substrate is being pulled with a velocity U , and a liquid film with constant thickness coats the substrate. An interesting property of this setup is that by altering the feed flow velocity V one can increase the critical value of U (beyond which wetting failure occurs) (Blake *et al.* 1999). This is the ‘hydrodynamic assist’ effect. The increase in the inertia of the impinging curtain causes an increase in

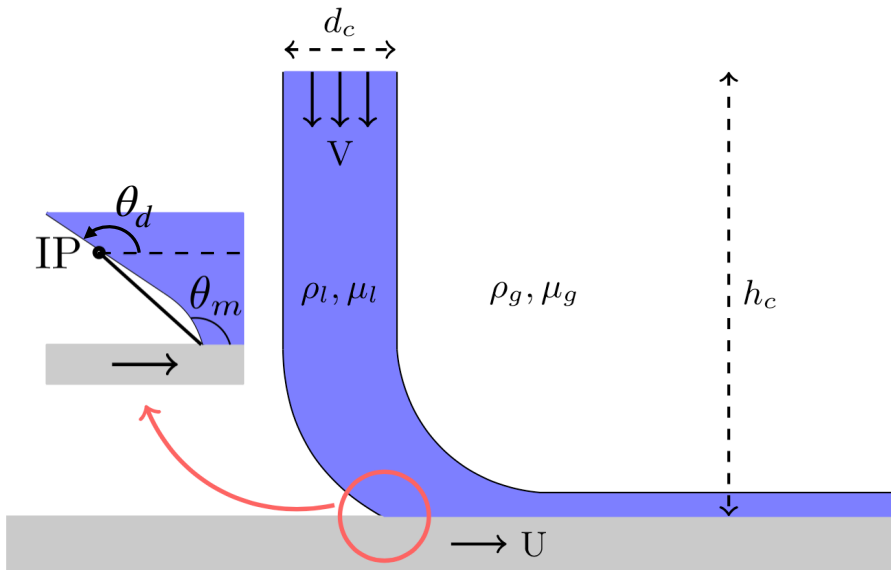


Figure 2: Schematic of the curtain coating configuration. The system parameters are h_c the curtain height, d_c the curtain width, ρ_l , ρ_g and μ_l , μ_g the densities and viscosities of the liquid phase and the gas phase respectively, U the substrate velocity, V the feed flow velocity and θ_m the imposed contact angle. The inflection point IP corresponds to the point at which the curvature of the interface is zero and the angle measured here is denoted by θ_d .

the pressure in the liquid in the vicinity of the contact line which ‘assists’ in pushing the air away from the contact line (Liu *et al.* 2016).

Wetting failure originates from the instability of the contact line and hence, the contact line dynamics are crucial to predicting the correct critical speed at the onset of wetting failure. As any fully resolved No-slip model can never predict any stable solutions of the dynamic contact line † (due to the discontinuity of the contact line velocity), the stable solutions are often studied numerically by the slip models along with an imposed constant microscopic contact angle (Chan *et al.* (2020), Kamal *et al.* (2019), Afkhami *et al.* (2009), Liu *et al.* (2016)). This procedure (use of slip model) was questioned by Wilson *et al.* (2006), Shikhmurzaev (2006) who performed simulations of the curtain coating setup using the slip boundary condition and neglecting the air phase. They tried to compare their numerical results against the experiments of Blake *et al.* (1999) and not only did the simulations fail to predict any critical wetting speed, but the variation in the dynamic or apparent contact angle was significantly narrower than observed in the experiments. Because of this, Wilson *et al.* (2006) concluded that the microscopic angle is also a function of macroscopic flow parameters like the Reynolds number based on the feed velocity. Later, Liu *et al.* (2016) demonstrated that assuming a constant contact angle at the grid scale and a slip boundary condition, while considering air stresses, one can predict some critical capillary number beyond which wetting failure happens. This would not have been possible with a free surface, where all capillary numbers result in a stable steady-state solution. Liu *et al.* (2016) tried this for a reduced setup with a ten-

† In VoF formulation, there is an implicit numerical slip, scaling with the grid size that removes the no-slip paradox and steady solutions are possible (Afkhami *et al.* 2009)

micron slip length and not for the parameters corresponding to the Blake experiments, which require nanometric slip lengths and hence huge computational costs.

However, the flow structure in the immediate vicinity of the contact line remains unclear. Experiments (Clarke 1995) show that the velocity along the interface increases as the contact line is approached down to the smallest observable scales (of order $20\ \mu\text{m}$). In contrast, viscous wedge solutions with slip predict a decrease of velocity towards the contact line (Hocking 1977). This discrepancy has been interpreted as evidence against slip-type models (Shikhmurzaev 2006). At the same time, the inertially corrected wedge analysis of Varma *et al.* (2021) predicts an increase of interfacial velocity when inertial effects are significant. In curtain coating, the local Reynolds number based on the distance from the contact line becomes order unity at micrometric scales, suggesting that inertia may control the observable flow even though the microscopic regularisation occurs at nanometric scales. Furthermore, different microscopic regularisations are known to produce nearly identical meniscus shapes at macroscopic distances (Dussan V. 1976). The present work investigates this possibility using direct numerical simulations of the two-phase Navier–Stokes equations with a Navier-slip boundary condition. Our objective is to determine which flow region selects the observable interface shape and velocity field, and how this connects microscopic regularisation to macroscopic behaviour. Our results show that qualitative macroscopic observations in rapidly advancing contact lines do not provide a decisive falsification of slip-type boundary conditions because the observable flow is controlled by hydrodynamic structure occurring outside the microscopic regularisation region. In other words, the supposed falsification is not decisive in this setup.

1.2. Overview of this paper

We first present the governing equations and numerical method used to simulate the two-phase curtain-coating configuration with a Navier-slip boundary condition. We then verify the numerical model by reproducing the reduced curtain-coating results of Liu *et al.* (2016) and by demonstrating convergence of the solution down to the slip-length scale, including numerical evidence of the logarithmic curvature singularity at the contact line (Kulkarni *et al.* 2023; Devauchelle *et al.* 2007). Next, we characterise the apparent contact angle measured at the inflection point located at micrometric distances from the contact line. We then analyse the velocity field along the interface and show that the experimentally observed acceleration near the contact line arises from an inertial region where the local Reynolds number is of order unity. The flow in this region is compared with the inertially corrected wedge solution of Varma *et al.* (2021), where the wedge angle is taken as the angle at the inflection point, and agreement improves as the slip length is reduced towards sub-micrometric values. Finally, we show that at larger scales the interface bending follows the Benney solution (Benney & Timson 1980). Together, these results indicate that the macroscopic interface shape is selected by the upstream flow rather than by the microscopic regularisation. Concluding remarks and perspectives are presented in §4.

2. Methodology

2.1. Mathematical model

The mathematical model is based on the mass and momentum conservation equations for incompressible and isothermal flow with variable density and surface tension force resulting in

$$\nabla \cdot \vec{u} = 0, \quad (2.8)$$

$$\frac{\partial \rho \vec{u}}{\partial t} + \nabla \cdot (\rho \vec{u} \vec{u}) = -\nabla p + \nabla \cdot (2\mu \mathbf{D}) + \vec{g} + f_\sigma, \quad (2.9)$$

$$\frac{\partial \rho}{\partial t} + \nabla \cdot (\rho \vec{u}) = 0, \quad (2.10)$$

where $\vec{u}(\vec{x}, t)$ is the velocity field and $p(\vec{x}, t)$ is the pressure field. The tensor \mathbf{D} is defined as $\frac{1}{2} [\nabla \vec{u} + (\nabla \vec{u})^T]$. ρ and μ are the density and viscosity respectively and \vec{g} is the acceleration due to gravity. f_σ is the surface tension force defined as

$$f_\sigma = \sigma \kappa \hat{\mathbf{n}} \delta_s(\vec{r} - \vec{r}_f), \quad (2.11)$$

which depends on the surface tension coefficient σ and the interface shape \vec{r}_f , particularly on its curvature κ and normal \vec{n}_s . The Dirac function $\delta_s(\vec{r} - \vec{r}_f)$ indicates that the force only acts at the interface and is zero everywhere else.

At the contact line, we assume a constant angle as in equation 1.1 and a Navier slip boundary condition for the fluid-solid interface. As mentioned in section 1, we impose the Navier slip boundary condition (NBC) (1.3).

2.2. Numerical method

We use the open source solver *Basilisk* (<http://basilisk.fr/>) developed at our institute by Stephane Popinet and various collaborators (Popinet (2009), Popinet (2015), Popinet (2018), Afkhami & Bussmann (2008), Afkhami & Bussmann (2009)). The two-phase interfacial flow capabilities of *Basilisk* focusing on the contact lines are well-tested (Afkhami *et al.* 2018; Fullana *et al.* 2020; Lācis *et al.* 2020). The reader can find a detailed description of the solver in the papers cited above. Here, we give a brief description.

A volume fraction field c is introduced, defined as 1 in fluid ‘1’ (liquid in this case) and 0 in fluid ‘2’ (gas). The interface is tracked by solving the advection equation for the volume fraction

$$\frac{\partial c}{\partial t} + \nabla \cdot (c \vec{u}) = 0. \quad (2.12)$$

The density and viscosity are then defined as

$$\rho = c\rho_1 + (1 - c)\rho_2. \quad \mu = c\mu_1 + (1 - c)\mu_2. \quad (2.13)$$

The contact angle boundary condition defines the normal vector at the contact line and hence affects the curvature calculation at the boundary and hence the calculation of the surface tension force. The contact angle is imposed at the boundary of the interface using a VoF tracer and the height function field, according to Afkhami & Bussmann (2008) approach. The reader is directed to Afkhami & Bussmann (2008) and Afkhami & Bussmann (2009) for full details. Briefly said, we define a ghost fluid layer below the domain and then set the tangential component of the height function field to give the desired normal vector at the contact line and hence the desired contact angle.

To numerically impose this boundary condition, we again use the ghost cells and specify the velocity in the ghost layer according to the following (equation 2.14) discretised form of the NBC (equation 1.3),

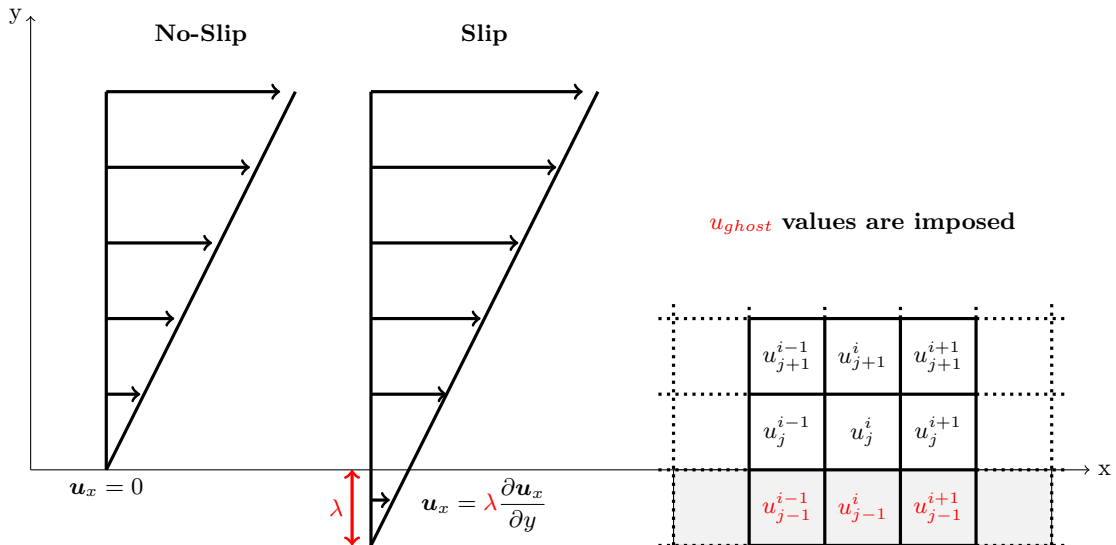


Figure 3: Visualisation of the slip length and numerical discretisation of the Navier slip boundary condition. The grey boxes below the x-axis are the ghost cells where the value is imposed according to equation (2.14).

$$\begin{aligned} \frac{\vec{u}_t[ghost] + \vec{u}_t[\]}{2} + \lambda \frac{\vec{u}_t[ghost] - \vec{u}_t[\]}{\Delta} &= \vec{U}_S \\ \iff \vec{u}_t[ghost] &= \frac{2\Delta}{2\lambda + \Delta} \vec{U}_{solid} + \frac{2\lambda - \Delta}{2\lambda + \Delta} \vec{u}_t[\]. \end{aligned} \quad (2.14)$$

Here $\vec{u}_t[\]$ is the tangential velocity of the fluid in the bottom layer and $\vec{u}_t[ghost]$ is the velocity in the ghost cell layer. Δ represents the grid size and λ is the slip length. This is visualised in the figure 3. The above implementation has been done in *Basilisk* by Tomas Fullana and tested by Fullana *et al.* (2020) and Lācis *et al.* (2020).

2.3. Simulations setup

The simulation setup is shown in figure 2. We define the Reynolds number, capillary number and Bond number as follows,

$$Re = \frac{\rho_l V d_c}{\mu_l}, \quad Ca = \frac{\mu_l U}{\sigma}, \quad Bo = \left(\frac{\rho_l g}{\sigma} \right) \left(\frac{d_c V}{U} \right)^2. \quad (2.15)$$

σ represents the surface tension and all other parameters are shown in figure 2. The gravity g is always assumed to be $9.81m/s^2$. To determine if we reach a steady state or not, we calculate the difference between the velocity field, the contact line position and the inflection point position at subsequent timesteps. If the difference for each of them is lower than a threshold, we conclude that a steady state is reached. For a given Re , we vary the Ca and predict a critical capillary number (Ca_{cr}) beyond which no steady-state solutions are found. The stability window is then deduced from the plot of the smallest Ca_{cr} for each Re .

To study the effect of slip length, we vary the slip length from 10 microns to a few

hundreds of nanometers. The resolution for the resolved slip length studies is reported in terms of grid size per slip length ($\frac{\lambda}{\Delta}$).

3. Results and discussion

The central issue of this paper is whether the micrometric flow features observed in curtain-coating experiments can be used to assess the validity of slip-type contact-line models. In particular, experiments show an apparent acceleration of the interfacial flow as the contact line is approached, whereas a purely viscous slip-regularised inner solution would predict deceleration inside the slip region (Shikhmurzaev 2006). In the curtain-coating configuration, however, the local Reynolds number at experimentally accessible distances is already of order unity, suggesting that the observed micrometric region may belong to an inertial intermediate scale rather than to the microscopic regularisation region.

We organise the results as follows. We first analyse the full curtain, then compare the interfacial velocity with the inertially corrected wedge solution and discuss the interface bending at larger scales. We then turn to the reduced configuration, where resolved-slip computations allow convergence studies, verification of the logarithmic singularity, and systematic exploration of the effect of slip-length reduction. Unless otherwise stated, all results use the reference parameter set of Liu *et al.* (2016), introduced later in §3.2.

3.1. The liquid curtain and the contact line flow physics

We begin with the full curtain-coating configuration in order to examine the flow structure near the advancing contact line in the complete two-phase setting. We first document the apparent acceleration in the full curtain simulations, then quantify it via the interfacial-velocity profiles and compare with the inertially corrected Stokes Flow Wedge solution (IC-SFW). This reveals that the apparent accelerating contact-line flow is an outer inertial structure which is truncated only inside the slip region, allowing the slip model and experimental observations to coexist without contradiction.

In the reference frame of the contact line, it is known (Moffatt 1964) that the Stokes flow wedge solution (SFW) for the three-phase contact line with a no-slip boundary condition gives the streamfunction $\Psi \sim rF(\alpha, \theta)$, where α is the wedge angle, r is the radial coordinate and θ is the angular coordinate assuming the contact line at the origin. Hence the velocity field depends on the angular coordinate and not on the radial coordinate. As a consequence, the SFW flow field is discontinuous at the contact line. From the analysis of Hocking (1977) and Kulkarni *et al.* (2023) in the flat-interface and liquid-vacuum limit, one can conclude that for the Navier-slip boundary condition, the velocity field varies linearly with the radial coordinate or the distance from the contact line, $u \sim r/\lambda$. This means that the velocity of the fluid decreases as one approaches the contact line and becomes exactly zero at the contact line, which makes the solutions presented by Hocking (1977) and Dussan V. (1976) for slip models continuous at the contact line.

Any Stokes flow subjected to a Navier-slip-like boundary condition will represent a no-slip-like solution in the far field and a slip model in the inner region. This indicates that the velocity along the interface in such a flow can only decrease up to the contact line. However, the experimental measurements for the curtain-coating setup by Clarke (1995) and Kistler (1984) show that the velocity along the interface increases up to the minimum resolution of the experiments, which was $20 \mu\text{m}$.

The increase in velocity can be attributed to inertia. We show now that, due to the high capillary number of the curtain-coating setup, inertial effects cannot be neglected

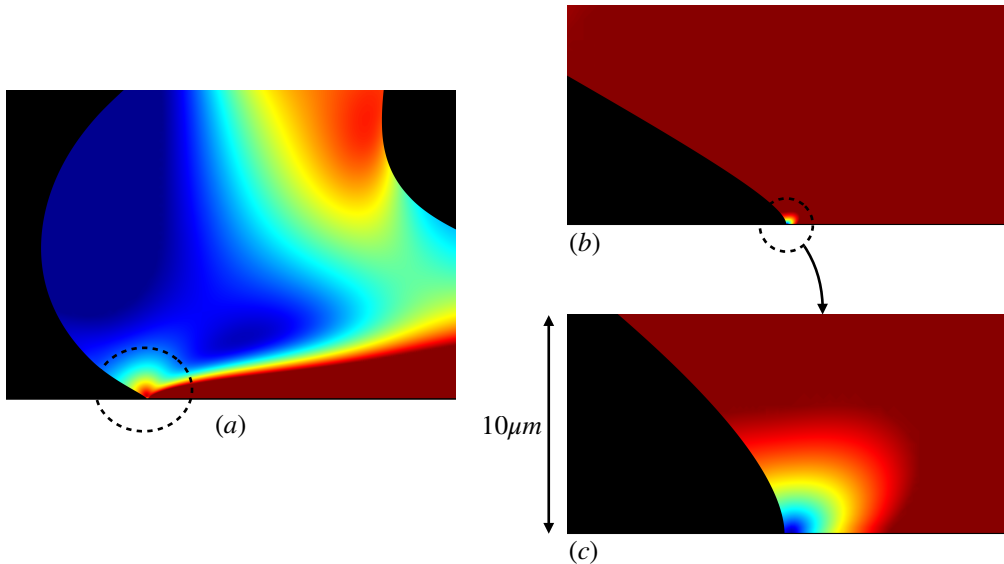


Figure 4: Zoom in at the contact line for the steady-state liquid curtain for $Re = 20$ and $Ca = 0.7$ in the laboratory frame of reference. The solid is moving from left to right and the contact line is at rest. Coloring is done by the magnitude of the velocity such that red is high and blue is low. It can be seen that at apparent scale the flow appears to accelerate as it approaches the contact line (a). Zooming in on the slip region (b,c), we see that the flow decelerates and the velocity approaches zero at the contact line (c). The slip length is $5 \mu\text{m}$.

even at a few tens of microns. Varma *et al.* (2021) solved the inertially corrected Stokes flow in a wedge (IC-SFW) subject to the no-slip boundary condition and found that the velocity field accelerates up to the contact line. In particular, Varma *et al.* (2021) showed that the velocity along the interface acquires a dependence on r . For an advancing contact line, the velocity magnitude along the interface for IC-SFW is smaller than the constant SFW value at a given angle, but approaches the SFW value at the contact line.

The relevant parameter is the local Reynolds number defined as $\bar{r} = \rho U r / \eta$, where U is the velocity of the contact line, r is the distance of a point in the fluid continuum from the contact line, and ρ and η are density and viscosity respectively. This \bar{r} is $\mathcal{O}(1)$ at $9 \mu\text{m}$ for the current setup assuming $Ca = 1$. For the experiments of Clarke (1995) ($U \sim 1\text{--}2 \text{ m s}^{-1}$, $\mu_l = 68 \text{ mPa s}$ and $\sigma = 61 \text{ mN m}^{-1}$), the value of \bar{r} is of order unity at tens of microns. This indicates that inertia cannot be neglected at the experimental resolution of $20 \mu\text{m}$.

Since we solve the two-phase Navier–Stokes equations, such effects are already present in our simulations. Figure 4 shows the steady-state liquid curtain colored by the velocity magnitude. We see that near the contact line, at apparent scale, the flow accelerates. This is identified by the red fan-like structure around the contact line in figure 4a. When we zoom in at the scale of the slip length, shown in figure 4c, only then do we see that the velocity magnitude starts to decrease, eventually approaching zero at the contact line, since this is a steady-state case. This is also seen in figure 5, where we plot isolines of the velocity magnitude: in the zoomed-out image 5(a), the contour values increase as the contact line is approached, whereas in the zoomed-in image they decrease. Hence the accelerating flow observed by Clarke (1995) and Kistler (1984) is not contradicting the

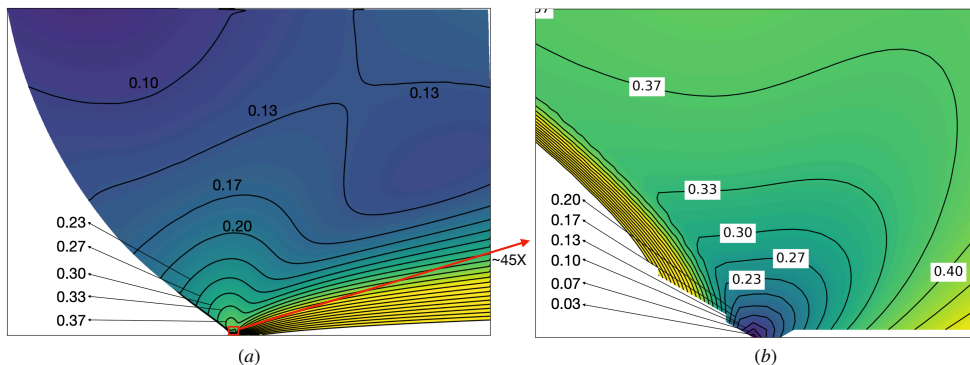


Figure 5: Contour plot showing the magnitude of the velocity field for figure 4. The labels indicate the speed magnitude of the contour lines. A fan-like structure is seen in the zoomed-out figure (a), where the magnitude is seen to increase as the contact line is approached. In the zoomed-in image (b), the speed contour values decrease up to the zero velocity at the contact line. The speed labels are scaled by the solid speed, taken to be 1.

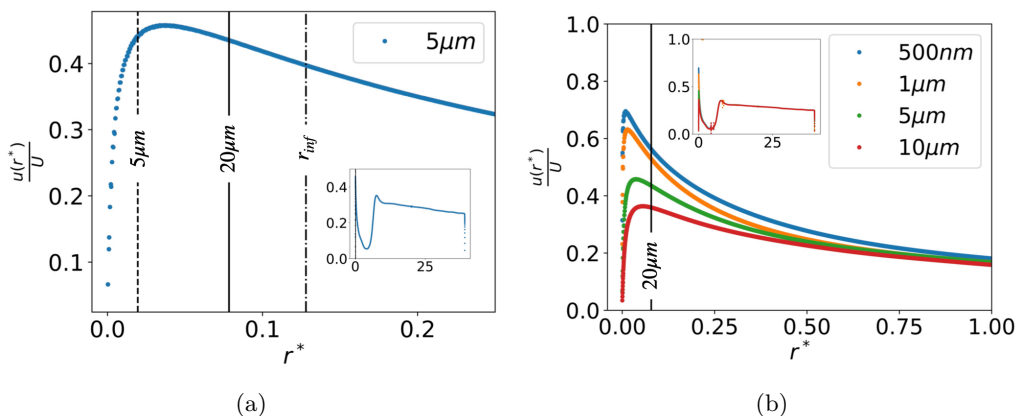


Figure 6: The velocity along the interface for $Re = 20$ and $Ca = 0.7$ for (a) $5\ \mu\text{m}$ slip length and (b) various slip lengths as indicated in the top-right inset. The inset figures (inset in (a), top-left inset in (b)) represent the full-scale behaviour and the main plot is a zoomed-in version near the contact line. The vertical $20\ \mu\text{m}$ line is the resolution of the experimental visualisation in Blake *et al.* (1999); Clarke (1995). r_{inf} is the position of the inflection point. U represents the plate velocity and r^* is the distance scaled with the coated film thickness.

slip model; it reflects the outer inertial structure, while the slip model regularises the flow only inside the slip-length region.

3.1.1. The velocity along the interface: The Varma solution[†]

We now examine the effect of inertia quantitatively. We plot the velocity along the interface in figure 6a. It is seen that (inset) the velocity initially has a slowly increasing plug-flow-like behaviour. It enters the neck region where it increases slightly, then enters

[†] In this section, the velocity is always defined in the reference frame of the contact line.

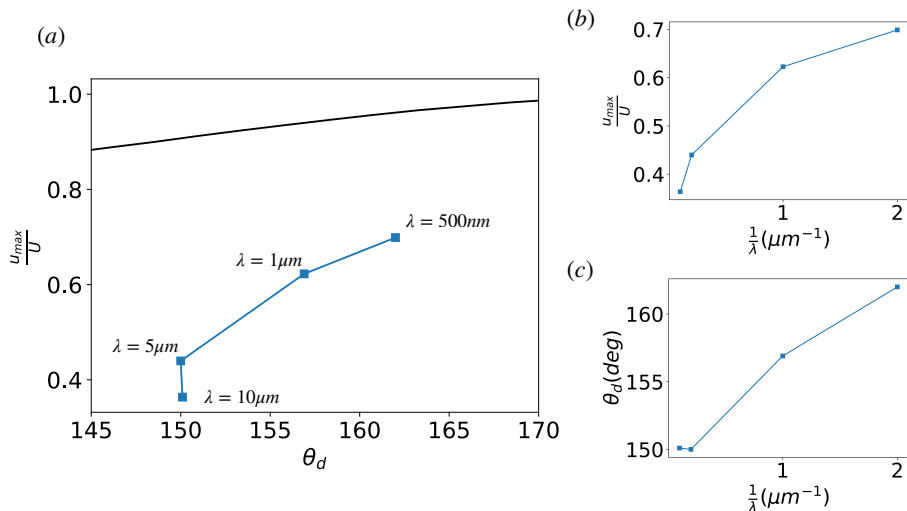


Figure 7: (a) The maximum value of the velocity along the interface u_{max} as a function of dynamic contact angle θ_d measured at the inflection point for various slip lengths λ . The solid black line represents the theoretical value calculated from the SFW solution. In this SFW solution we set the wedge angle equal to θ_d . The SFW solution serves as an upper bound for u_{max} . Values are scaled by the solid plate speed U . Plots (b) and (c) represent the variation of u_{max} and θ_d with the slip length respectively. The \bar{r}_{inf} , local Reynolds number based on the inflection-point distance, is **2.36** for $\lambda = 10\mu\text{m}$ and **0.44** for $\lambda = 500\text{nm}$.

the bump region where it slows down and finally starts to increase rapidly. This is in exact coherence with the experimental observations of Clarke (1995). When the distance from the contact line is less than a few microns, below the experimental resolution of Clarke (1995), we see the effect of the slip boundary condition: the velocity starts to decrease and finally goes to zero at the contact line.

The rapid increase before entering the slip region is caused by inertia. The IC-SFW solution of Varma *et al.* (2021) for an advancing contact line with a no-slip boundary condition predicts an increase in velocity along the interface reaching the SFW value at the contact line. Since we have a non-zero slip length, we see that the increase in velocity is not up to the SFW limit, but to a certain value below it. As we further reduce the slip length, we see an increase in the maximum velocity value, as shown in figure 6b.

In figure 7 we plot the maximum value of the velocity as a function of slip length and also the dynamic contact angle measured at the inflection point. Figure 7(b) indicates that the maximum velocity increases as the slip length decreases and figure 7(c) shows that the dynamic contact angle measured at the inflection point also increases as the slip length decreases. In the SFW solution with no-slip boundary condition, the constant value of the velocity along the interface increases with wedge angle. Taking the wedge angle equal to the inflection-point angle of our simulation, the constant value of the velocity along the interface calculated from the SFW solution should serve as an upper bound for the maximum value obtained in our simulations. In figure 7(a) we compare the numerical maximum velocity with the analytically obtained SFW value. We see that the maximum is indeed bounded by the SFW value, and the difference decreases as the slip length is reduced.

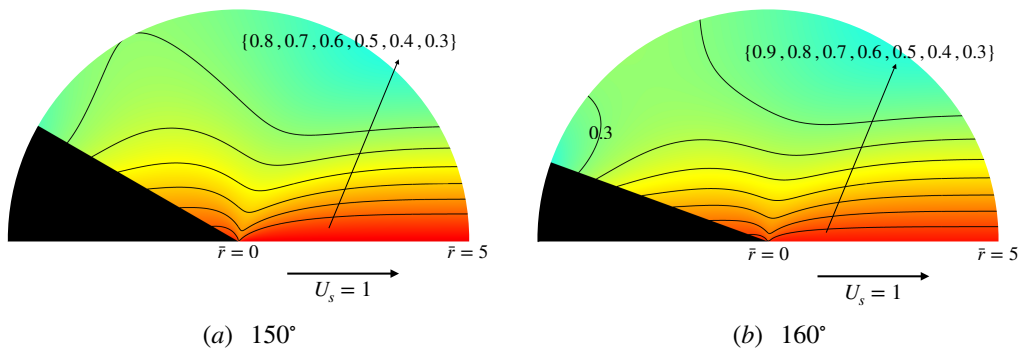


Figure 8: The numerical solution for IC-SFW for two different wedge angles. The contour map shows the coloring by the velocity magnitude and the isolines show that the flow accelerates as we approach the contact line. The bottom wall is the no-slip wall moving with velocity $U_s = 1$ and the inclined edge represents the free surface. Simulations are 2D and \bar{r} is the local Reynolds number used as dimensionless distance.

We now show that at an apparent scale outside the slip region (a few tens of microns), the flow can be described by the IC-SFW, with the wedge angle equal to the inflection-point angle. The steady-state Navier–Stokes equation can be written in streamfunction formulation as

$$\Delta^2 \Psi(\bar{r}, \theta) = \frac{1}{\bar{r}} \left(\frac{\partial \Psi}{\partial \theta} \frac{\partial (\Delta \Psi)}{\partial \bar{r}} - \frac{\partial \Psi}{\partial \bar{r}} \frac{\partial (\Delta \Psi)}{\partial \theta} \right), \quad (3.16)$$

where \bar{r} is the local Reynolds number as well as the dimensionless distance and θ is the angular coordinate. The contact line is at $\bar{r} = 0$. Note that equation (3.16) with RHS= 0 is the SFW equation. This equation was analytically solved by Varma *et al.* (2021) in a wedge with $\theta = 0$ (interface) to $\theta = \alpha$ (no-slip moving solid plate). Once the streamfunction is obtained for \bar{r} and θ , the velocity along the interface can be calculated as a function of \bar{r} . Analytical solutions were not possible for wedge angle $\alpha > 0.715\pi$ ($\sim 130^\circ$), leaving only numerical means.

Hence we numerically solve the IC-SFW equation (3.16) using *Basilisk*. The numerical IC-SFW solutions for wedge angles 150° and 160° are shown in figure 8. We see that the flow field accelerates up to the contact line. The final value of the velocity along the interface obtained at the contact line for the IC-SFW solution must match the SFW solution. This is verified in Appendix B.

We extract the velocity along the interface from the numerical IC-SFW solution for the wedge angle equal to the inflection-point angle and compare it against the full curtain setup. Since we have a slip boundary condition on the entire solid surface, it is not reasonable to use the actual solid speed values directly in this comparison. IC-SFW is a no-slip solution, whereas due to slip at the fluid-solid surface the effective velocity felt by the fluid in the full curtain is smaller than the solid plate velocity. Hence, we scale the velocity field with the u_{max} obtained from figure 7a (blue squares). Note that in the physical setup the slip length would be a few nanometers, so the effect of slip would be negligible at a few tens of microns; in our setup the slip length is of the order of microns, so this effective velocity correction must be taken into account.

The final comparison for the scaled velocity of the IC-SFW numerical solution with the full curtain solution is shown in figure 9. We see that as the slip length is decreased, the full curtain velocity profile approaches the numerical IC-SFW solution at the micrometre

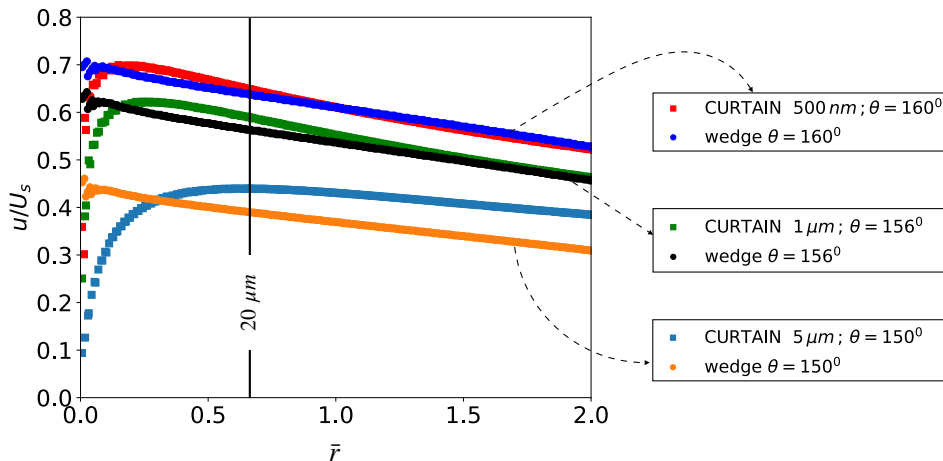


Figure 9: Comparison for the velocity along the interface for the numerically obtained IC-SFW wedge solution against the full curtain-coating simulation. The value of θ is the inflection-point angle for the full curtain-coating setup and is also the corresponding wedge angle for the IC-SFW solution.

scale. We cannot perform resolved-slip simulations at slip lengths smaller than 500 nm due to the time-step limitation.

3.1.2. Bending at an intermediate scale: The Benney solution

We now discuss the interface bending observed in the curtain profiles at an intermediate scale. In the previous subsection we focused on the increase in velocity along the interface and its consistency with the inertial correction of Varma *et al.* (2021). Here we focus on the interface shape and show that an intermediate region of the curtain profile is well described by the classical free-surface Stokes-flow solution of Benney & Timson (1980).

For the no-slip boundary condition and 180° contact angle, Benney & Timson (1980) solved the Stokes-flow equation for a free surface and derived a solution for the interface shape in polar coordinates. The final solution up to leading order, with the help of an illustrative sketch in figure 10, for the streamfunction and interface shape is written below. We call this *the Benney solution*,

$$\begin{aligned} \Psi(r, \theta) = -Ca r \sin \theta + ar^q \left(\frac{2-q}{2} Ca \cos q\theta \right. \\ \left. + \frac{2-q}{4} \sin q\theta + \frac{q}{2} Ca \cos(q-2)\theta + \frac{q}{4} \sin(q-2)\theta \right), \end{aligned} \quad (3.17)$$

$$\theta(r) = ar^{q-1}, \quad (3.18)$$

where

$$\tan(q\pi) = -2 Ca. \quad (3.19)$$

For finite stress, one must have $q > 1$. For the smallest allowable values, this gives two ranges for q , i.e. $1 < q < 3/2$ for the receding contact line and $3/2 < q < 2$ for the advancing contact line. Note that the actual solution of Benney & Timson (1980) contains a sign mistake in equation (2.12) of their paper for the normal pressure term, which interchanges the range of q for the advancing and receding cases. This error, to the best of our knowledge, was first noticed by Ngan & Dussan V. (1984).

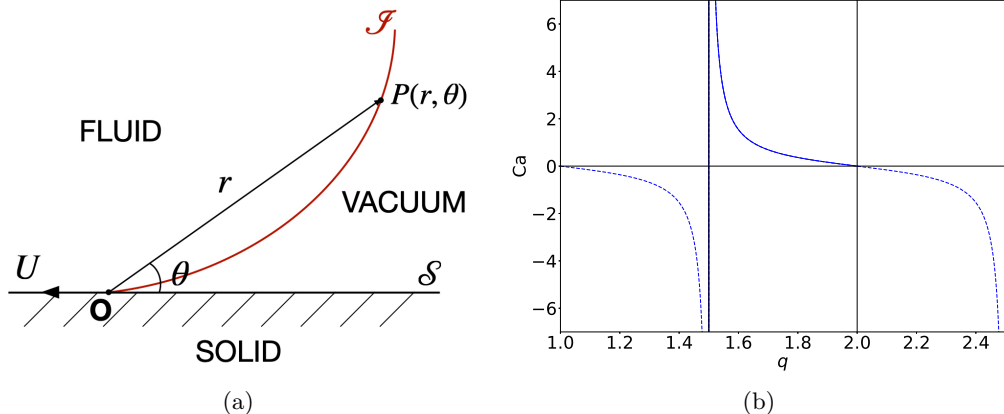


Figure 10: Schematic illustration of the Benney solution. (a) The polar-coordinate notation. Interface \mathcal{I} is a free surface and makes a 180° contact angle with the solid surface \mathcal{S} at origin \mathbf{O} . The solid is pulled towards the left and hence the setup is an advancing contact line. (b) The solution branch for the Benney solution for the advancing contact line, $q \in (3/2, 2)$, is the solid line in the plot.

Due to the presence of a free parameter, the prefactor a of equation (3.18), Ngan & Dussan V. (1984) concluded that the problem is ill-posed. Later researchers, however, showed that the prefactor is determined by matching with the outer flow, giving evidence that the Benney & Timson (1980) solution holds well for the innermost scale of a theoretical no-slip boundary condition and 180° contact angle, or at an intermediate scale, especially for $Ca \sim \mathcal{O}(1)$, for which innermost details like the grid-scale contact angle and the slip length do not matter. For details on such works, one can refer to Benilov & Vynnycky (2013) for a Couette flow with a free surface and Kamal *et al.* (2019) for a plunging plate with a free surface. For the full derivation of the Benney solution, one can refer to the original paper of Benney & Timson (1980) (noting the sign mistake), or the version of Kamal *et al.* (2019).

We show the flow field obtained from the streamfunction solution (3.17) in figure 11. Note that the contact angle is 180° and since the no-slip boundary condition is satisfied on the solid plate, the velocity of the contact line is not zero; in fact, it is equal to the plate velocity. This does not lead to any discontinuity or singularity, because here the contact line is not a material line and performs a rolling motion. Figure 11b shows the increase in velocity along the interface up to the curvature, and one concludes that the increase is negligible as compared to what we see in figure 6b and in the experiments of Clarke (1995). Beyond the values of r displayed, the interface has turned enough (figure 11a) that the Benney solution limit is lost. The prefactor a is taken to be unity for both figures.

As we have a system with a small density and viscosity ratio, we check how our interface shape compares with the Benney solution in figure 12. We see that the solid line of the Benney solution fits well to the simulation. Note that for small angles, we can assume $\theta = y/x$ and $r = x$; hence the Benney solution $\theta \sim r^{q-1}$ becomes $y \sim x^q$. To visually show the physical region where we see the Benney solution in our full curtain profile, we plot the interface shape and corresponding Benney solution in figure 13. In figure 13(a) we use a log-log scale to show the fitting, whereas in figure 13(b) we use a linear scale to

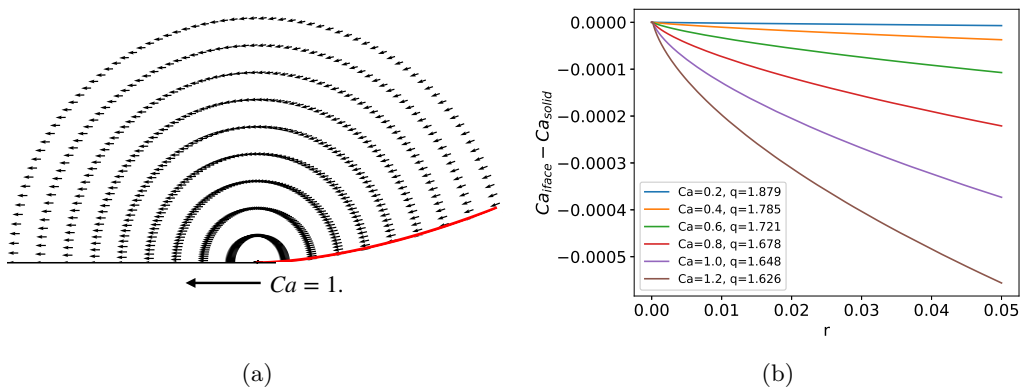


Figure 11: (a) Flow field and interface profile (red) obtained for $Ca = 1$ and $a = 1$ from the streamfunction given in equation (3.17). (b) The capillary number based on the velocity along the interface in the Benney solution as a function of r . The legend represents the capillary number based on the solid plate velocity and the corresponding exponent q .

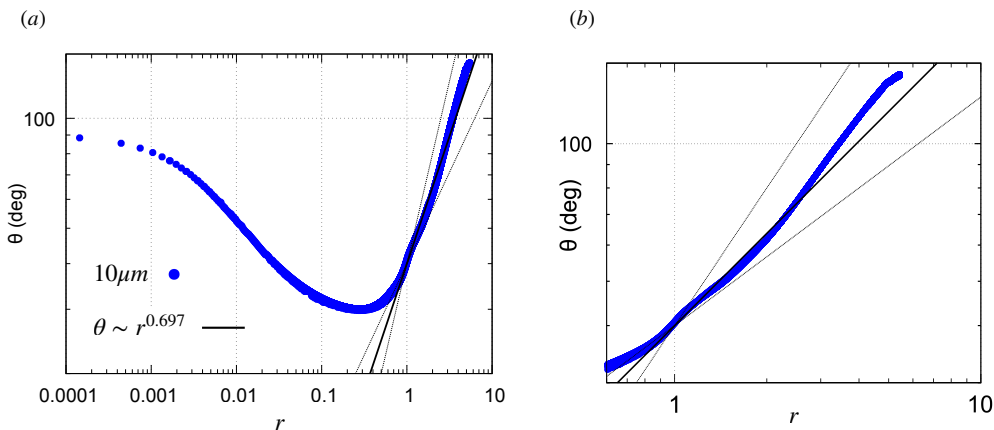


Figure 12: Interface profile in r - θ coordinates to represent the Benney solution. The distance r is scaled by the coated film thickness h_{inf} . The blue points correspond to the full curtain simulation with $Re = 20$ and $Ca = 0.7$ and slip length of $10\mu\text{m}$, which is $0.047h_{inf}$. The solid line represents $\theta = ar^{q-1}$ with the value of q found from equation (3.19) in the branch $q \in (3/2, 2]$ for $Ca = 0.7$. The dotted lines are $\theta \sim r^{0.5}$ and $\theta \sim r^1$ to represent the limiting range of the exponent $(q - 1)$ for $Ca \rightarrow \infty$ and $Ca = 0$ respectively. The full profile is shown in (a) while (b) shows the zoomed-in region of the fit from (a).

show the Benney region more directly. Note that θ in the Benney solution is a coordinate and should not be confused with the angle in figure 24a, where it was a local slope.

In appendix E.2 of Varma *et al.* (2021), the effect of interface bending is compared with inertial effects. It is seen that for parameters in the range of our study and above the scale of $20\mu\text{m}$, inertial effects are dominant and interface bending only negligibly affects

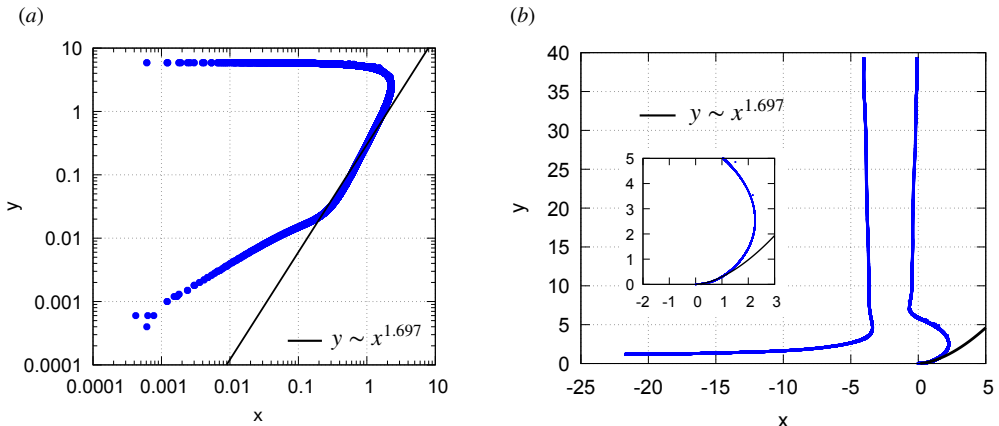


Figure 13: The x - y interface profile for figure 12 for better visualisation of the Benney solution. The contact line is taken as the origin and (a) shows the Benney solution fit in x - y coordinates where the exponent q is based on $Ca = 0.7$, same as in figure 12. The coordinates are again scaled by h_{inf} . (b) The interface profile in linear scales as it appears practically. The solid black line is the Benney solution. The entire plots (a) and (b) are the same except that (a) is on a log-log scale while (b) is on a linear scale.

the increase in velocity along the interface. Both the solutions of Benney & Timson (1980) and of Varma *et al.* (2021) have as zeroth-order term the no-slip Stokes flow with locally planar interface. The leading-order correction term added by Benney & Timson (1980) causes a quantifiable interface bending and a negligibly small increase in the velocity along the interface. The leading-order inertial correction terms added by Varma *et al.* (2021) cause a quantifiable increase in velocity along the interface, and negligible bending. These two corrections therefore represent distinct higher-order perturbations to the same zeroth-order Stokes-wedge structure and can coexist without contradiction over the experimentally relevant intermediate scales. We hence conclude that the increase in velocity along the interface comes from inertial effects, whereas the interface bending comes from the Benney & Timson (1980) solution. As stated in the beginning, this is subject to further work and lies beyond the scope of this paper.

3.2. Hydrodynamic assist and stability in the curtain configuration

We now present the results of our simulations using the reference parameters of Liu *et al.* (2016). We have the following parameters (symbols are as per figure 2 and σ is the surface tension):

$$\begin{aligned}
 \rho_l &= 1000 \text{ kg/m}^3, & \mu_l &= 25 \text{ mPa s}, & d_c &= 1 \times 10^{-3} \text{ m}, \\
 \rho_g &= 1.2 \text{ kg/m}^3, & \mu_g &= 0.018 \text{ mPa s}, & h_c &= 1 \times 10^{-2} \text{ m}, \\
 \sigma &= 70 \text{ mN m}^{-1}, & \theta_m &= 90^\circ, & \lambda &= 1 \times 10^{-5} \text{ m}.
 \end{aligned}$$

These parameters are useful for two reasons. First, the relatively large slip length λ makes the computations cheaper and, more importantly, enables *resolved-slip* simulations in which the slip region is explicitly resolved rather than represented implicitly by a grid-dependent effective slip length. This allows us to probe the near-contact-line structure and to perform controlled convergence studies. The limitation is that such a large λ is

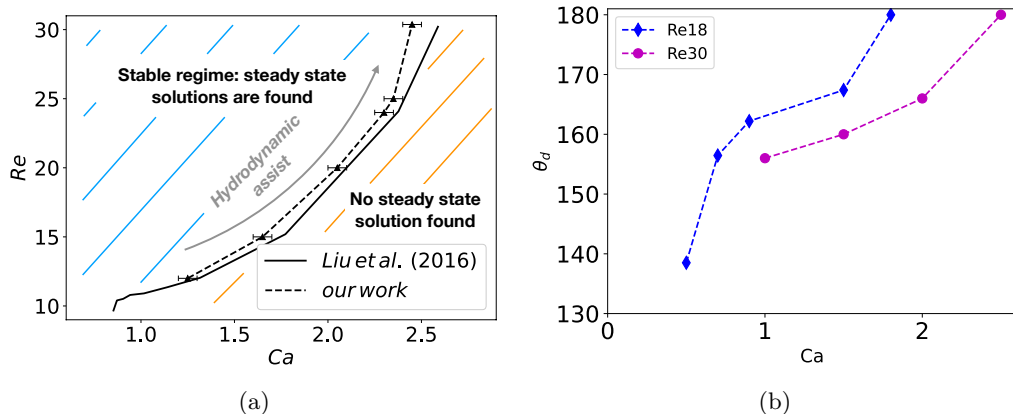


Figure 14: (a) Comparison of the stability window obtained in the current simulations against the previous simulations of Liu *et al.* (2016). The curves indicate the critical capillary number above which wetting failure takes place and no steady-state solutions are found. The left portion of the bifurcation curve refers to the stable regime where steady-state solutions are found. (b) Macroscopic contact angle θ_d measured at the inflection point as a function of Ca for different Re for the reduced model. The values on the y-axis are in degrees and a variation of more than 20° is clearly seen for various Re .

not intended for quantitative comparison with experiments; in particular, at high Ca it does not guarantee that inertia is negligible at the slip-length scale, unlike the physical nanometric-slip situation. For this reason we later perform slip-length reduction down to our computational limits.

Figure 14a compares our stability boundary with that reported by Liu *et al.* (2016). We recover the hydrodynamic-assist trend: increasing the feed flow (larger Re) delays wetting failure, i.e. increases the critical capillary number Ca_{cr} over a substantial portion of parameter space. The agreement is notable because Liu *et al.* (2016) modelled the gas stresses using a reduced one-dimensional description, whereas we solve the full two-phase Navier–Stokes equations; the close match in the low- Re , low- Ca regime supports the accuracy of their gas-stress model in that limit.

We next consider the apparent contact angle measured at the interface inflection point, located a few tens of micrometres (20–50 μm) from the contact line. At this position the curvature changes sign and the local slope varies slowly, making it a natural proxy for the experimentally observed macroscopic angle (Voinov 1976). In slip-based descriptions with a prescribed microscopic angle, the inflection point represents an intermediate scale

$$\lambda < r_{inf} < r_{macro},$$

where capillary pressure reverses sign to deflect the gas phase away from the contact line and sustain steady wetting. In experiments such as Blake *et al.* (1999), where λ is nanometric, this location lies well below optical resolution ($\sim 20 \mu\text{m}$). In the present reduced model ($\lambda = 10 \mu\text{m}$), however, the inflection-point angle provides a convenient macroscopic proxy that can be consistently extracted from the simulations and compared with experimentally reported apparent angles.

Figure 14b shows that this angle depends not only on the capillary number but also on the large-scale Reynolds number. At fixed Ca , variations of several tens of degrees are observed, consistent with the trends reported by Blake *et al.* (1999). The crossing of constant- Re curves indicates a non-monotonic dependence on Re . The dashed black

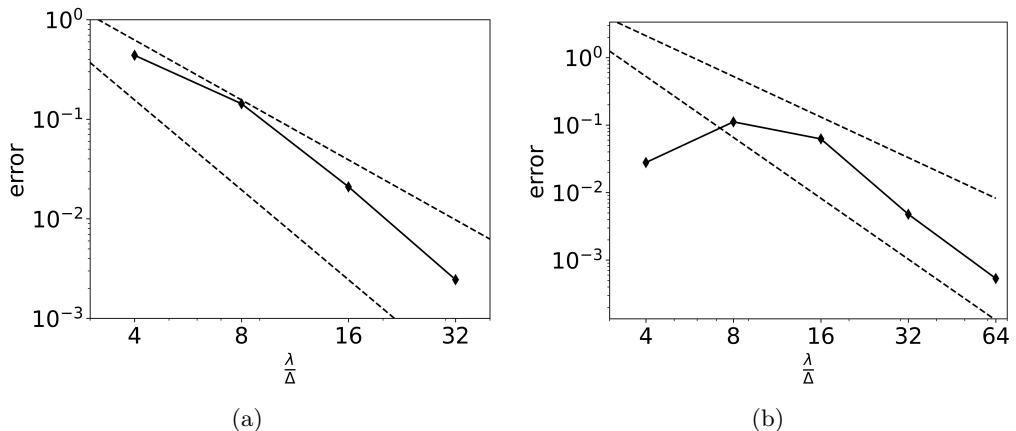


Figure 15: (a) Convergence study for the contact line position. $\frac{\lambda}{\Delta}$ denotes the number of grid points per slip length. The error on the y-axis is $(x - x_{ref})$ where x is the contact line position for a given $\frac{\lambda}{\Delta}$ and x_{ref} is the reference solution for 64 grid points per slip length. The dotted lines show order-2 and order-3 convergence. (b) Convergence study for the dynamic contact angle measured at the inflection point. The error on the y-axis represents $\left(\frac{\theta_d - \theta_d^{ref}}{\theta_d^{ref}} \times 100\% \right)$ where θ_d^{ref} is the reference solution for 128 grid points per slip length. The plots are for the reduced curtain model $Re = 20$ and $Ca = 0.7$, where a steady-state solution is obtained.

curve marks the stability boundary: wetting failure does not necessarily occur when the angle reaches 180° . Instead, for a given Re , the angle increases with Ca up to a critical value ($\leq 180^\circ$) beyond which no steady solution exists. The observation of $\theta_{inf} < 180^\circ$ at the transition is consistent with both molecular-dynamics and continuum studies (Keeler *et al.* 2022; Liu *et al.* 2016).

Having characterised the steady solutions and their stability boundary, we now use the reduced model to verify that the resolved-slip numerics capture the known inner logarithmic singular structure, and to assess how the stability window changes when the slip length is varied.

3.2.1. The curvature singularity

The Navier-slip formulation is known theoretically to possess a logarithmic (integrable) pressure and curvature singularity at the moving contact line (Kulkarni *et al.* 2023; Devauchelle *et al.* 2007). The objective of this subsection is therefore not to infer the existence of the singularity, but to verify that the present resolved-slip simulations correctly capture this inner asymptotic structure.

Because the slip length is explicitly resolved, the solution must converge with the number of grid points per slip length $N = \lambda/\Delta$, unlike approaches where the slip is implicitly determined by the grid size ($\sim \Delta/2$). Figure 15 shows convergence of both the contact-line position and the inflection-point angle with approximately third-order accuracy, demonstrating that the near-contact-line region is numerically resolved. Additional refinement-level diagnostics, including the progressive improvement of the VoF reconstruction and the local angle/curvature behaviour near the contact line, are given in Appendix C.

As the grid is refined, the contact angle at the wall converges to the imposed value

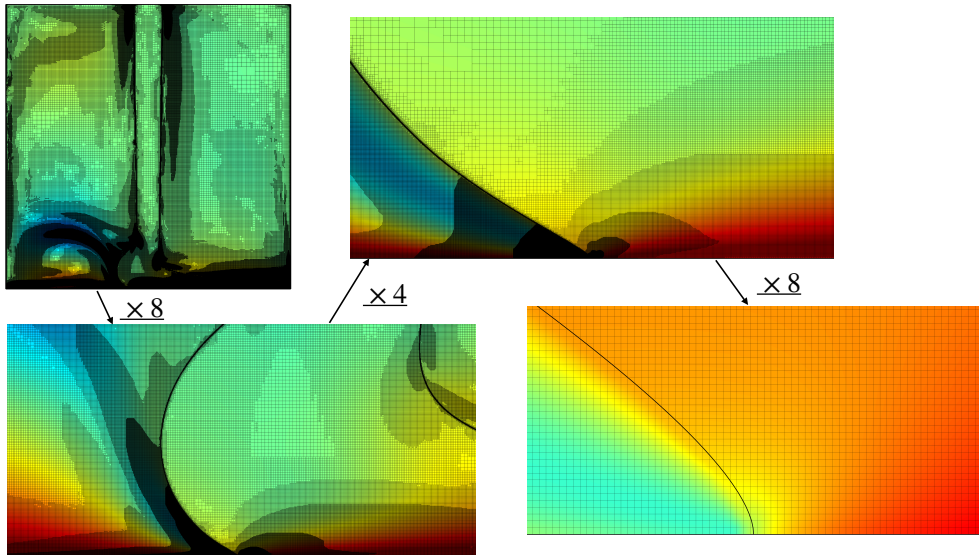


Figure 16: Successive zoom-in near the contact line in a steady-state simulation of $Re = 20$ and $Ca = 0.7$. Mesh refinement can be seen and the background is colored by the horizontal velocity.

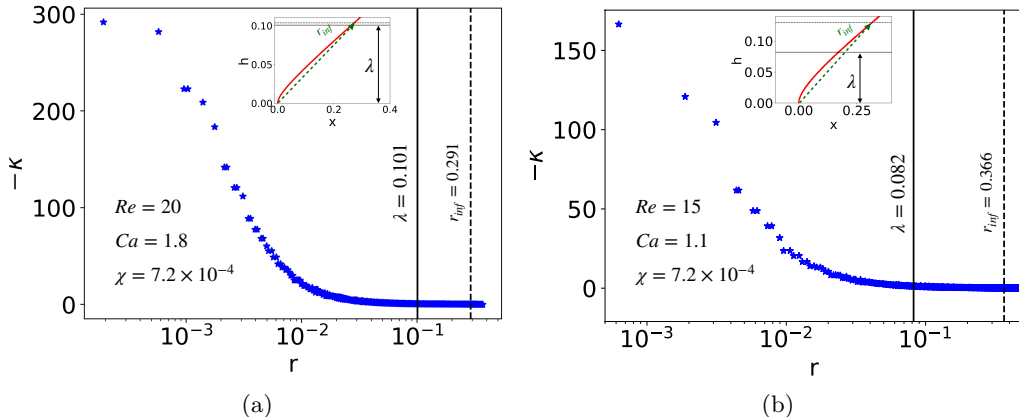


Figure 17: Logarithmic divergence of the curvature at the contact line. The inset shows the zoomed-in plot of the interface in the vicinity of the contact line $(0, 0)$. The dashed line represents the position of the inflection point and the solid line represents the slip length. The plots are for (a) critical capillary number and (b) sub-critical capillary number.

of 90° , while its gradient grows without bound, as shown in Appendix C. Thus the interface remains locally straight at the contact line while becoming non-smooth there. This is precisely the behaviour expected from the integrable logarithmic singularity of the Navier-slip model in the Stokes-flow limit. A successive zoom-in near the contact line is shown in figure 16.

Figure 17 directly shows the logarithmic divergence of curvature. Because the singularity is integrable, the wall shear stress remains finite and steady solutions exist despite the

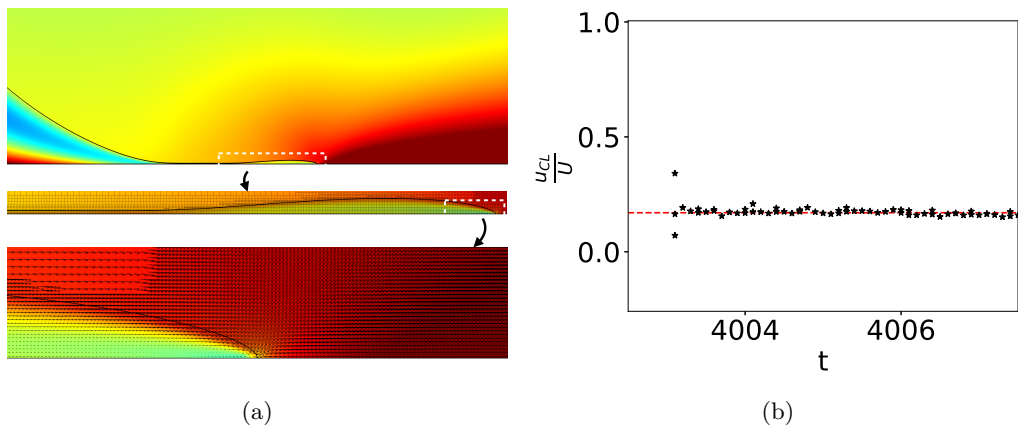


Figure 18: Wetting failure case for $Re = 20$ and $Ca = 2.0$ with $10\ \mu\text{m}$ slip length and 64 grid points per slip length. (a) Zoom in near the advancing air-film cusp. The background is colored by u velocity and velocity vectors are shown in the most zoomed-in version. (b) The contact-line velocity (cusp tip) as a function of time. Time is non-dimensional and the horizontal red-dashed line is $y = 0.17$.

divergence. Notably, near the stability limit the height of the inflection point approaches the slip length, indicating a possible loss of scale separation at the onset of wetting failure.

3.2.2. Film entrainment during wetting failure

We consider an unstable case of the reduced model ($Re = 20$, $Ca = 2$). Instead of approaching a steady state, the interface develops an entrained air film with a cusp-like shape that propagates along the plate (figure 18). The apparent angle measured at the inflection point becomes reflex, indicating loss of a steady coating solution. A notable feature is that the cusp tip rapidly reaches an approximately constant velocity in the laboratory frame, about 17% of the plate speed (figure 18b). Wetting failure therefore corresponds to the replacement of a stationary contact line by a steadily propagating entrainment front.

3.2.3. Effect of the slip length reduction

Experiments report a non-monotonic stability window, whereas the reduced model with a large slip length yields a monotonic behaviour for hydrodynamic assist on an Re – Ca plane. We therefore progressively reduce the slip length toward physically realistic values to examine how the stability window evolves.

Figure 19a shows the evolution of the critical capillary number Ca_{cr} as the slip length decreases for several Reynolds numbers. As λ is reduced, the solution branches cross and the stability boundary becomes non-monotonic: increasing Re does not always increase Ca_{cr} . This behaviour is clearly visible in the stability diagram (figure 19b). The monotonic trend observed for $\lambda = 10\ \mu\text{m}$ disappears at smaller slip lengths ($1\ \mu\text{m}$ and $500\ \text{nm}$), where a non-monotonic stability window emerges.

A complementary study of the influence of the imposed microscopic contact angle on the large-scale angle measured in the heel configuration is reported in Appendix D.

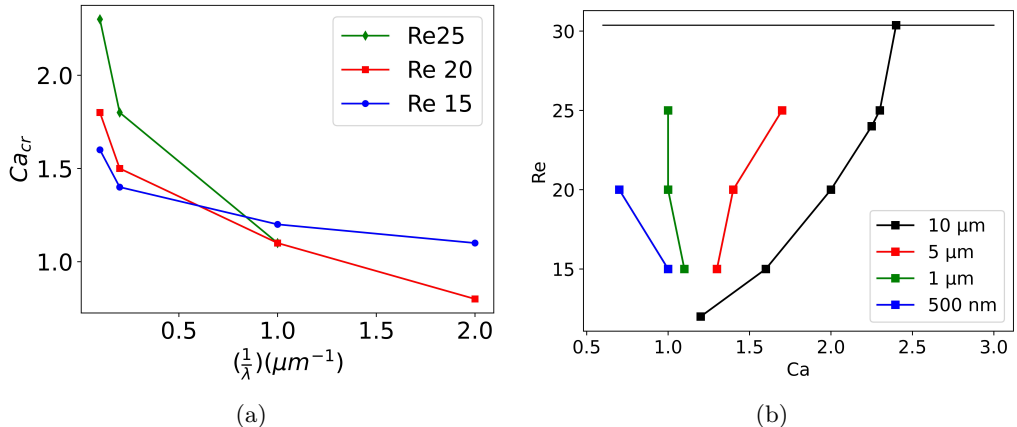


Figure 19: (a) Critical capillary number as a function of slip length for various Reynolds numbers indicated in the legend. (b) The stability window shifting with the reduction of the slip length.

4. Conclusion

We have presented the full 2D description of the curtain-coating setup governed by the two-phase Navier–Stokes equations with a Navier-slip boundary condition and a constant contact angle at the grid scale. The simulations predict a critical capillary number for wetting failure and provide strong numerical evidence for the logarithmic curvature singularity. We validated the results against the previous computations of Liu *et al.* (2016), who used a one-dimensional model for air stresses. The simulations also qualitatively reproduce the experimentally observed non-monotonic stability window and the non-local variation of the macroscopic contact angle measured at the inflection point.

One critical aspect of this study is explaining the accelerating flow observed at scales of a few tens of micrometres from the contact line, and showing that it does not contradict the slip model. Consider the local Reynolds number defined as $\bar{r} = \rho_l U r / \mu$. This is $\mathcal{O}(1)$ for $r \sim 10 \mu m$ when $Ca = 1$, so inertial effects cannot be neglected at this scale. In section 3.2 we saw that the macroscopic angle at a few microns, and in section 3.1.1 the velocity along the interface, are both strongly influenced by inertia. To justify quantitatively that it is inertia which causes the accelerating flow field, we compared the increase in velocity observed in the full curtain setup against the numerically solved IC-SFW solution. We showed that, when the wedge angle is taken equal to the angle observed at the inflection point, the IC-SFW solution works reasonably well and improves as the slip length is decreased. Also, we have evidence that the nanoscopic slip-length solution, which causes a decrease in velocity only in the immediate vicinity of the contact line ($r < \lambda$), does not influence the bending at the scale of a few microns. This is consistent with the appearance of a Benney-like (Benney & Timson 1980) solution at the micrometre scale. Since the Benney solution completely ignores microscopic physics such as the grid-scale contact angle and the slip region, it must apply in the asymptotic limit where the inner slip-region physics has been eliminated[†]. We can thus conclude that the distance from where we start seeing this solution is the distance from where one can ignore the inner slip-region physics, at least for describing the interface bending.

[†] For example, region II in Kamal *et al.* (2019).

It is worthwhile to note that the highest level of grid refinement used was Basilisk level 17, which implies that the ratio of smallest grid size to domain size is 2^{17} . This means that our full two-phase simulations span five orders of magnitude, which is already enormous given that we perform transient simulations with both phases. This ratio is, however, still lower than the full centimetre-to-nanometre ratio of experiments, which corresponds to seven orders of magnitude. Since we wanted to fully resolve the slip-length region, we used slip lengths of the order of microns for most of the study, allowing sufficient grid points inside the slip region.

While our results provide valuable insights, there are also several important logical deductions that we now emphasise:

1. *The curtain-coating setup does not provide a decisive falsification of the slip-length model.*

The curtain-coating problem is particularly challenging because it involves $Ca \sim \mathcal{O}(1)$. This leads to the formation of the inflection point quite close to the contact line and often below the experimental resolution of $20 \mu\text{m}$. The results obtained here show, at least qualitatively, that a slip-type model can reproduce the wetting-failure parameters, the interfacial velocity field and the interface bending up to the experimental resolution. Thus, in a Popperian sense, the macroscopic observations available in this setup do not decisively falsify the Navier-slip or mobility-law model.

2. *For $Ca \ll 1$ and local Reynolds number $\bar{r} \ll 1$, slip-like models are expected to work.* This is the regime where one expects the Cox law (Cox 1986), or its generalisation to arbitrary angles by Chan *et al.* (2020), to apply. Unlike curtain coating, this regime leads to inflection points formed at experimentally observable micrometric scales, for example in pulling-plate setups. This is because for $Ca \rightarrow 0$, there is no strong bending in the vicinity of the contact line and hence no nearby inflection point.

3. *Observations at the $20 \mu\text{m}$ scale are insufficient to prove or disprove the microscopic regularisation for $Ca \sim \mathcal{O}(1)$ and $\bar{r} \ll 1$.*

The observation referred to here is the measurement of the interface shape or angle indicating the bending. In reality, one expects the slip regularisation to act at nanometric scales, whereas the angle measurements are done at a few microns. Hence, there may be multiple models that regularise the flow in the inner region while preserving the same interface bending at the micrometre scale. This was also argued analytically by Dussan V. (1976), where different inner-region boundary conditions lead to substantially different inner flows but the same bending at the meniscus scale.

4. *To test whether the fluid behaves exactly as predicted by the slip model would require measurements below the micrometre scale.*

Although this is challenging experimentally, one possible future direction is to compare simulations using slip-like boundary conditions with molecular-dynamics simulations. This has been done recently by Lācis *et al.* (2022) for a nanoscale shear-droplet setup. One could further want to do such studies for setups where large separation of scales is not present, while steady solutions with $Ca \sim \mathcal{O}(1)$ are still possible.

One could, for example, study the interface bending in a thin-channel flow where a denser liquid is pushed into a vacuum or ambient gas by a pressure gradient. This would result in an advancing contact line with $Ca \sim \mathcal{O}(1)$ even for steady-state

solutions.†

5. A mathematically ill-posed continuum model can remain useful only if it is weakly singular and does not introduce sub-continuum scales.

For example, in the plunging-plate problem of Kamal *et al.* (2019), the Stokes equations subject to the slip boundary condition and a constant contact angle predict a finite but very large curvature at the contact line. The radius of curvature in that case was a hundred ($Ca = 1.01$) or ten thousand ($Ca = 1.81$) times smaller than the slip length. Although such a model may preserve macroscopic physics correctly, it is inconsistent at smaller scales. We have seen that the curvature in our case diverges logarithmically despite using the same definition of the slip model as Kamal *et al.* (2019). Hence, the difference could come only from the fact that Kamal *et al.* (2019) assumed a free surface whereas we consider a full two-phase flow. This indicates that there is a possibility that the slip model is singular at zero viscosity ratio, although this needs to be further examined. It may appear counter-intuitive to suggest that a weakly singular curvature model is more reasonable than a finite-curvature model, but this is because a finite radius of curvature may itself introduce an additional length scale much smaller than the slip length, causing the inflection point to appear inside the slip region where the continuum assumption breaks down.

6. There is circumstantial evidence that the slip-length model remains compatible with the observed macroscopic behaviour.

In particular, it predicts wetting failure and preserves the inertial effects responsible for macroscopically observed features such as interface bending and the accelerating velocity field in the vicinity of the contact line.

Despite this, the model is weakly singular and thermodynamically ill-posed, which leaves open the possibility of finding better contact-line models in the future. Finally, we feel that the present work is a useful step toward the search for a well-posed dynamic contact-line model in the continuum sharp-interface limit. It is also a first step towards full DNS of the experiment for a rapidly advancing contact line.

We acknowledge the support of the ERC grant TRUFLOW nr 883849. We are grateful for access to the computational facilities of the French CINES (National computing centre for higher education) and the TGCC granted by GENCI under project number A0092B07760. The project also benefited from the PRACE grant TRUFLOW number 2020225418 for a large number of CPU hours in 2021. We thank the technical and administrative teams of these supercomputer centres and agencies for their kind and efficient help. We also acknowledge the computational grant on the Swiss computer Piz Daint.

We would like to thank Michele Pellegrino, Petter Johansson, Sherwin Bagheri, Berk Hess and Gustav Amberg for the monthly group meetings where several ideas on the contact line flowed freely.

Stephane Zaleski would like to thank Yves Pomeau, Jens Eggers and Yulii Shikhmurzaev for detailed discussions.

Yash Kulkarni would like to thank Mathis Fricke, Dieter Bothe and Jens Eggers for the discussions.

† This setup would be schematically similar to Keeler *et al.* (2022), but only with advancing contact lines.

Appendix

A. Temporal and spatial discretisation of the Navier–Stokes solver

(This is just an overview. The reader is directed to Tryggvason *et al.* (2011) for the detailed procedure.) Our Navier–Stokes solver uses a staggered discretisation of the volume-fraction/density and pressure combined with a time-splitting projection method. The discretised form of the equations appears as below:

$$\rho_{n+\frac{1}{2}} \left(\frac{\vec{u}_* - \vec{u}_n}{\Delta t} + \vec{u}_{n+\frac{1}{2}} \cdot \vec{\nabla} \vec{u}_{n+\frac{1}{2}} \right) = \vec{\nabla} \cdot \left[\mu_{n+\frac{1}{2}} (D_n + D_*) \right] + (\sigma \kappa \delta_s \vec{n})_{n+\frac{1}{2}} + \vec{g}_{n+\frac{1}{2}}. \quad (\text{A } 1)$$

$$\frac{c_{n+\frac{1}{2}} - c_{n-\frac{1}{2}}}{\Delta t} + \vec{\nabla} \cdot (c_n \vec{u}_n) = 0 \quad (\text{A } 2)$$

$$\vec{u}_{n+1} = \vec{u}_* - \frac{\Delta t}{\rho_{n+\frac{1}{2}}} \vec{\nabla} p_{n+\frac{1}{2}} \quad (\text{A } 3)$$

Note that \vec{u}_* is a temporary velocity field, which is found in the first step (equation A 1) by ignoring the pressure-gradient term in the momentum equation (2.9). Then the pressure-gradient term is added to get the final velocity field. This two-step procedure is known as the predictor–corrector projection method. To solve for the pressure gradient and ensure a divergence-free velocity field, equation (A 3) is coupled with the Poisson equation

$$\vec{\nabla} \cdot \left[\frac{\Delta t}{\rho_{n+\frac{1}{2}}} \vec{\nabla} p_{n+\frac{1}{2}} \right] = \vec{\nabla} \cdot \vec{u}_*. \quad (\text{A } 4)$$

Now the discrete form of the momentum equation (A 1) can be rearranged as follows:

$$\frac{\rho_{n+\frac{1}{2}}}{\Delta t} \vec{u}_* - \vec{\nabla} \cdot \left[\mu_{n+\frac{1}{2}} \vec{D}_* \right] = \vec{\nabla} \cdot \left[\mu_{n+\frac{1}{2}} \vec{D}_n \right] + (\sigma \kappa \delta_s \vec{n})_{n+\frac{1}{2}} + \rho_{n+\frac{1}{2}} \left[\frac{\vec{u}_n}{\Delta t} - \vec{u}_{n+\frac{1}{2}} \cdot \vec{\nabla} \vec{u}_{n+\frac{1}{2}} \right]. \quad (\text{A } 5)$$

This scheme is solved by the second-order upwind Bell–Collela–Glaz advection scheme (Bell *et al.* 1989).

Space is discretised using a quadtree partitioning in 2D (octree in 3D), as shown in figure 20. All variables are collocated at the centre of each square discretisation volume. Consistently with a finite-volume formulation, the variables are interpreted as the volume-averaged values for the corresponding discretisation volume. A projection method (Popinet 2003) is used for the spatial discretisation of the pressure-correction equation and the associated divergence in the Poisson equation.

B. Numerical IC-SFW solution and matching

The analytical IC-SFW solution of Varma *et al.* (2021) is available only up to the critical angle of $\sim 0.715\pi$, that is around 130° . Hence beyond the critical angle, we are left with only numerical means. We use the embedded-boundary method in 2D to create a wedge and solve the full Navier–Stokes equations until a steady state is reached. The no-slip boundary condition is imposed using a Dirichlet boundary condition on the domain boundary (solid wall) and the embedded boundary (fluid interface) is kept at a symmetry boundary condition to represent the free surface. The details of implementing Dirichlet

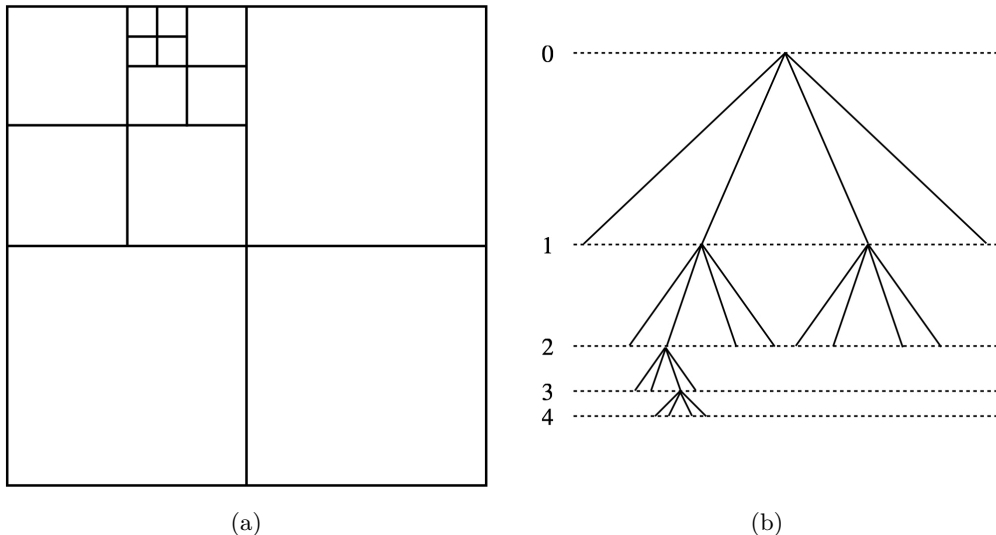


Figure 20: (a) Illustration of quadtree adaptive mesh refinement. (b) The tree representation.

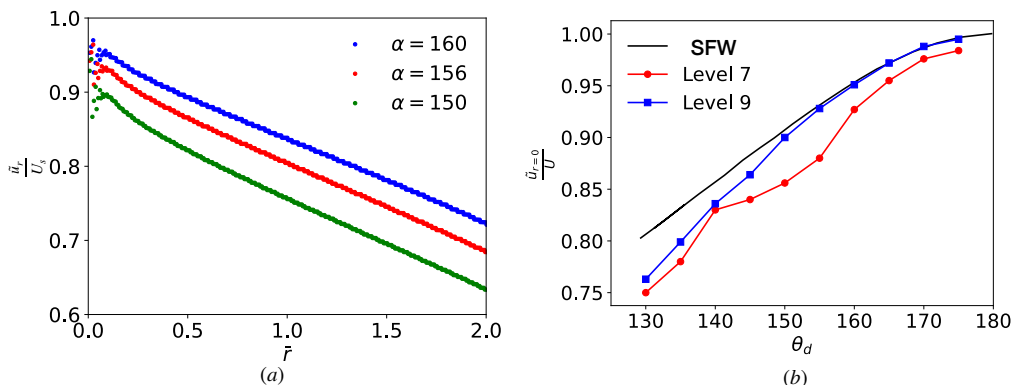
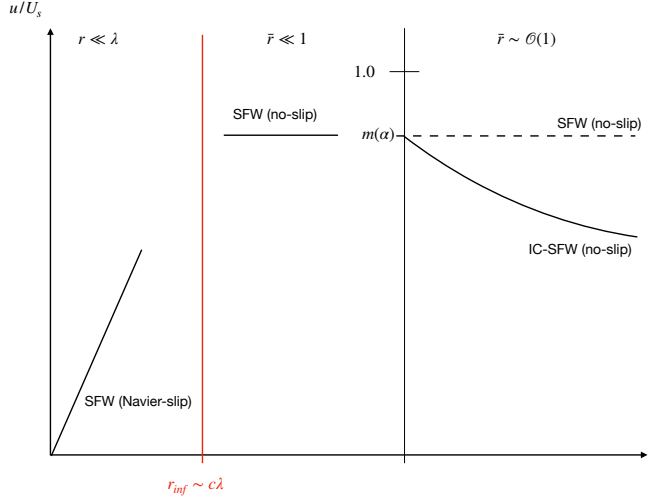


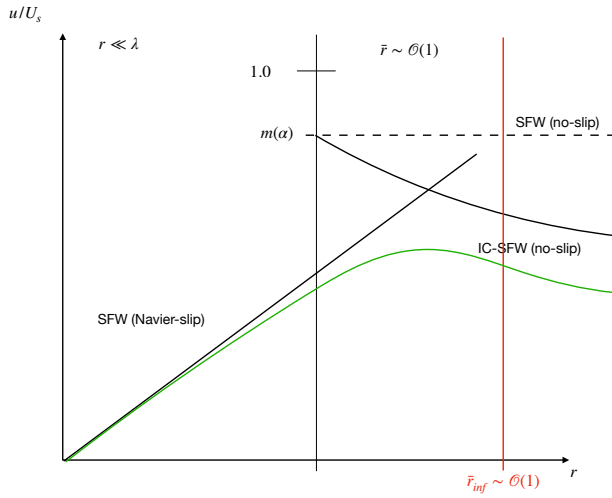
Figure 21: (a) The velocity along the interface for the Basilisk IC-SFW solution for three wedge angles as a function of local Reynolds number \bar{r} . Note that the noise at $\bar{r} = 0$ is numerical as numerics do not allow a discontinuous velocity field. (b) The value of the velocity at $\bar{r} = 0$ (five grid cells away from the contact line to avoid noise at the wall) in the IC-SFW solution of (a) is extracted for each wedge angle and compared against the analytical SFW solution. Level 7 represents a mesh of $2^7 \times 2^7 = 16384$ cells in the computational domain up to $\bar{r} = 10$ and Level 9 corresponds to a mesh of $2^9 \times 2^9 = 262144$ grid points.

and Neumann boundary conditions can be found on <http://basilisk.fr/src/embed.h> and are based on the scheme of Johansen & Colella (1998).

The effect of adding inertia causes an increase in velocity along the interface that is otherwise absent in the SFW solution. This increase is up to the Stokes-flow value for a given wedge angle. In figure 21(a) we show the variation of the velocity along the interface as obtained from our numerical IC-SFW solution. Extracting the limiting value of the



(a)



(b)

Figure 22: Schematic of the asymptotic behaviour of the velocity along the interface in the vicinity of the contact line in the reference frame of the contact line. \bar{r} is the local Reynolds number and λ is the slip length. The constant $m(\alpha)$ depends on the wedge angle α and varies from 0 at $\alpha = 0$ to 1 at $\alpha = \pi$. Subfigure (a) shows the asymptotic behaviour expected if the local Reynolds number based on the inflection point is small enough. Subfigure (b) shows the behaviour if the local Reynolds number based on inflection-point distance is not small enough, which is the case in the present work. This causes us to scale the velocity profiles in figure 6b to u_{max} .

velocity in our IC-SFW simulation, we compare it with the theoretically obtained SFW value in figure 21(b) for various wedge angles. We see good agreement as we refine the grid.

In the schematic figure 22 we show how the asymptotics are expected to work. The IC-SFW causes velocity to increase up to the SFW value, which depends on the wedge angle. Finally, it decreases to zero as we enter the slip region. Note that U_s is the speed of the fluid particle at the fluid-solid interface. In an ideal case, where the slip length is small enough to yield an inflection point close to the contact line such that the local Reynolds number based on the inflection-point distance satisfies $\bar{r}_{inf} \ll 1$, we expect the velocity along the interface to behave like figure 22a. That is, we expect the velocity along the interface predicted by the IC-SFW solution to exactly match the full curtain region when $\bar{r} \sim \mathcal{O}(1)$. However, in our case, the inflection-point location yields $\bar{r}_{inf} \sim \mathcal{O}(1)$, hence we expect a behaviour like figure 22b. That is, the velocity along the interface qualitatively behaves similarly to that predicted by the IC-SFW solution, but requires scaling down due to the interference of the slip region. This encourages further work with smaller slip lengths. One could thus imagine the inflection-point distance as an indicator of how far slip-length effects extend.

C. Additional resolved-slip diagnostics

Figure 23 shows the progressive improvement of the VoF reconstruction and the local flow field near the contact line as the slip region is increasingly resolved due to mesh refinement.

The main text establishes the logarithmic curvature singularity through figure 17. We now provide additional numerical diagnostics showing how this singular behaviour looks with the mesh refinement. Although the curvature diverges at the contact line, the interface angle at the wall still converges to the imposed value. In other words, the interface remains locally tangent to the wall with the prescribed contact angle, while the rate at which that angle changes becomes unbounded as the contact line is approached.

Figure 24 makes this structure more explicit. In figure 24a, the extracted wall angle converges to the imposed value of 90° as the grid is refined. However, the slope profile becomes increasingly steep in the immediate vicinity of the contact line. Equivalently, the derivative of the angle, and hence the curvature, grows without bound. This is shown directly in figure 24b, where the curvature extracted closer and closer to the contact line increases systematically with refinement.

This behaviour is the numerical signature of a logarithmic curvature singularity. The singularity is weak (or integrable) that the interface remains locally flat at the contact line in the sense of its tangent direction, yet the second derivative diverges. Thus, the contact line may still be viewed locally as having the imposed contact angle, even though the curvature at that same point is unbounded. This is precisely the structure demonstrated in the main text through figure 17.

D. Effect of the microscopic grid-scale contact angle on the large-scale angle in the heel configuration

We examine whether the macroscopic contact angle measured a few tens of microns from the contact line is controlled by the imposed microscopic contact angle. This also clarifies why the free-surface simulations of Wilson *et al.* (2006) did not reproduce the experimentally observed interface bending of Blake *et al.* (1999).

We consider a heel configuration ($Re = 30$, $Ca = 0.7$) and restart from a steady

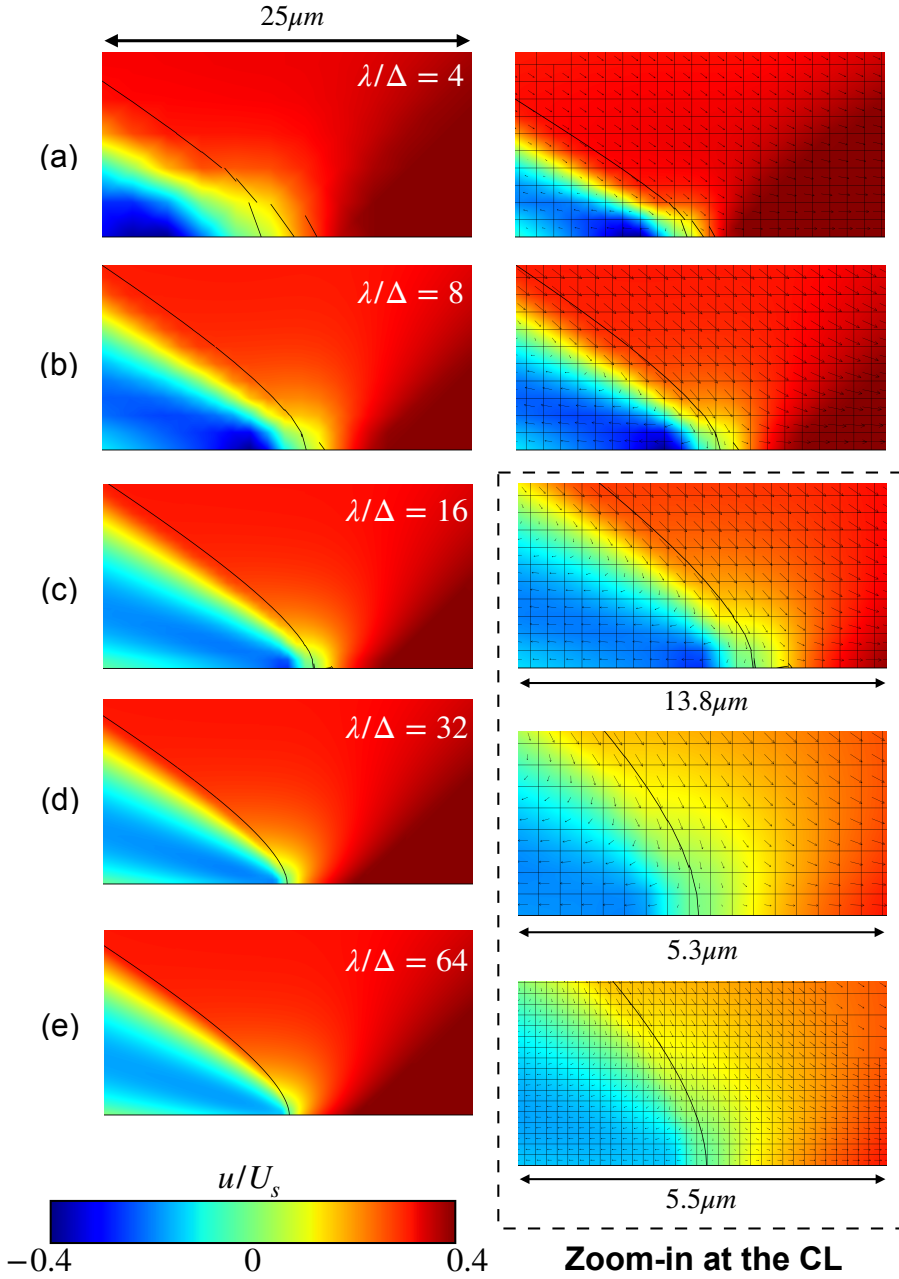


Figure 23: Zoom in near the contact line for $Re = 20$ and $Ca = 0.7$. The horizontal velocity colors the background and the velocity vectors are shown. The resolution in terms of grid size per slip length is (a) $\frac{\lambda}{\Delta} = 4$, (b) $\frac{\lambda}{\Delta} = 8$, (c) $\frac{\lambda}{\Delta} = 16$, (d) $\frac{\lambda}{\Delta} = 32$, and (e) $\frac{\lambda}{\Delta} = 64$. At maximum grid refinement, the grid size is 160 nm.

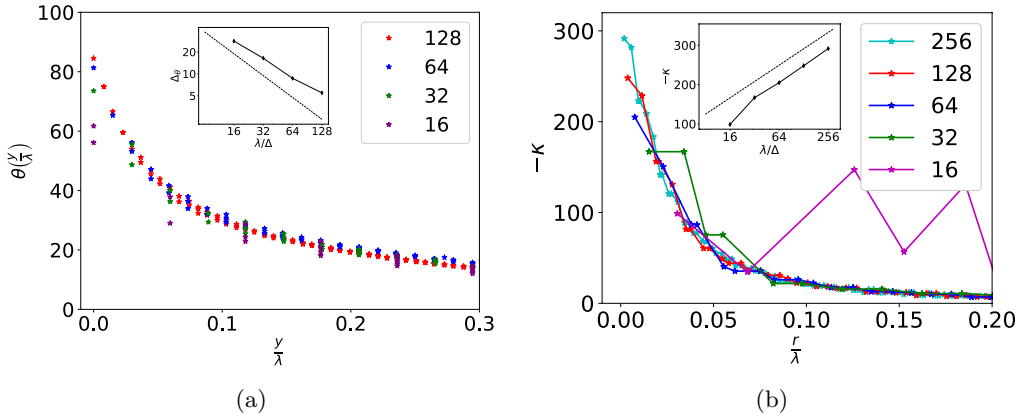


Figure 24: (a) Angle or local slope as a function of the vertical distance from the contact line. The inset shows the value of the extracted contact angle in the contact-line cell. (b) Curvature as a function of radial distance from the contact line. The inset shows the extracted curvature from the contact-line cell. Both plots are for $Re = 20$ and $Ca = 1.8$. The legend represents the number of grid points per slip length in both cases.

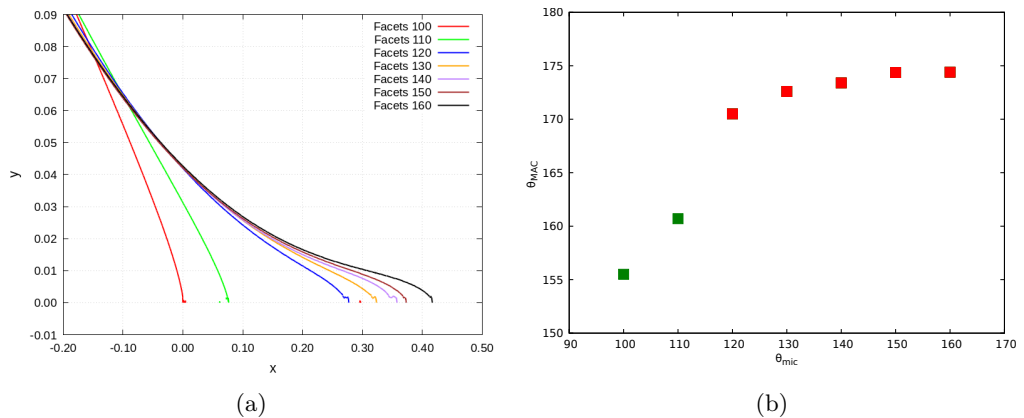


Figure 25: (a) Interface shapes near the contact line for the reduced model with $Re = 30$ and $Ca = 0.7$. The axes are non-dimensionalised with the entrained film thickness as in the rest of the paper. The slip length is $10\mu\text{m}$, which is 0.038 in the scaled unit. Only the interface shapes corresponding to 100° and 110° are steady-state solutions. The rest are unstable. (b) Macroscopic contact angle measured at $20\mu\text{m}$ from the contact line. Green squares indicate that a steady-state solution is obtained and red ones are unsteady. The resolution is 16 grid points per slip length.

solution obtained with a microscopic angle of 90° . The microscopic angle is then varied between 100° and 160° . No steady solution exists for imposed angles above 120° . Figure 25a shows the interface shapes after relaxation, where only the 100° and 110° cases reach steady state.

Figure 25b reports the apparent angle measured at $20\mu\text{m}$ from the contact line. When a steady solution exists, the macroscopic angle varies weakly (about 5° – 7°) despite large changes in the microscopic angle. This variation is smaller than the experimental uncertainty reported by Blake *et al.* (1999). In contrast, when no steady state exists, the

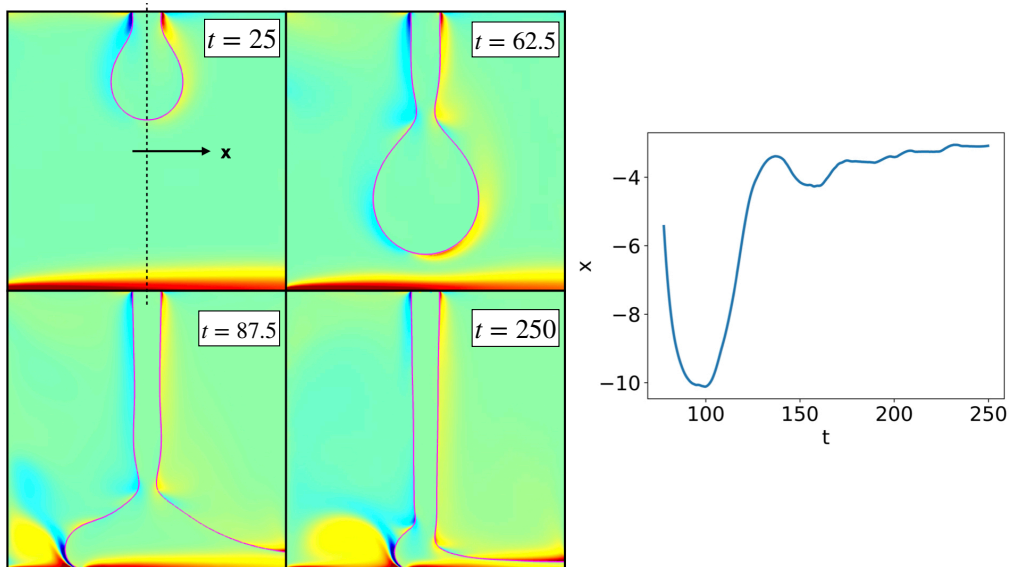


Figure 26: Chronology of the liquid curtain relaxing to a steady state for $Re = 20$ and $Ca = 0.7$ for the reduced model (section 3.2). The plate is being pulled to the right and we are in the laboratory frame of reference. The time is scaled by the viscous time scale given by $T = \frac{\mu l}{\rho_l h_c^2}$ and the background is colored by the vorticity field. The plot on the right shows the position of the contact line formed as a function of time.

apparent angle approaches 180° and film entrainment occurs. Wetting failure is therefore qualitatively different from a steady coating solution rather than a continuation of it.

The free-surface simulations of Wilson *et al.* (2006) used a microscopic contact angle of 165° . This directly places them in an unstable regime for the physical two-phase system. However, in a single-phase free-surface formulation with Navier slip, steady solutions exist for arbitrarily large Ca and imposed angles. As a result, the apparent angle remains close to 180° and varies only weakly, leading to a discrepancy with the experimentally measured angle at tens of microns from the contact line.

E. The DNS chronology of the liquid curtain

Figure 26 shows a chronology of reaching the steady state where the liquid curtain falls and a contact line is formed when the liquid impinges on the substrate. The liquid then spreads on the substrate due to inertia and the contact line moves towards the left in the laboratory frame of reference, reaches a maximum (seen as the minimum in the plot) and then moves towards the right, in the direction of the solid substrate velocity, and relaxes to a steady-state position after a few small back-and-forth oscillations. Note that the transient dynamics are out of the scope of this paper and we restrict attention to the steady-state description only.

REFERENCES

- AFKHAMI, S., BUONGIORNO, J., GUION, A., POPINET, S., SAADE, Y., SCARDOVELLI, R. & ZALESKI, S. 2018 Transition in a numerical model of contact line dynamics and forced dewetting. *J. Comput. Phys.* **374**, 1061–1093.

- AFKHAMI, S. & BUSSMANN, M. 2008 Height functions for applying contact angles to 2D VOF simulations. *Int. J. Numer. Methods Fluids* **57**, 453–472.
- AFKHAMI, S. & BUSSMANN, M. 2009 Height functions for applying contact angles to 3D VOF simulations. *Int. J. Numer. Methods Fluids* **61**, 827–847.
- AFKHAMI, S., ZALESKI, S. & BUSSMANN, M. 2009 A mesh-dependent model for applying dynamic contact angles to VOF simulations. *J. Comput. Phys.* **228** (15), 5370–5389.
- BELL, J. B., COLELLA, P. & GLAZ, H. M. 1989 A second-order projection method for the incompressible navier–stokes equations. *J. Comput. Phys.* **85** (2), 257–283.
- BENILOV, E. S. & VYNNYCKY, M. 2013 Contact lines with a 180° contact angle. *J. Fluid Mech.* **718**, 481–506.
- BENNEY, D. J. & TIMSON, W. J. 1980 The rolling motion of a viscous fluid on and off a rigid surface. *Stud. Appl. Math.* **63** (2), 93–98.
- BLAKE, T. D., BRACKE, M. & SHIKHMURZAEV, Y. D. 1999 Experimental evidence of nonlocal hydrodynamic influence on the dynamic contact angle. *Phys. Fluids* **11** (8), 1995–2007.
- BLAKE, T. D. & HAYNES, J. M. 1969 Kinetics of liquid–liquid displacement. *J. Colloid Interface Sci.* **30** (3), 421–423.
- BLAKE, T. D. & SHIKHMURZAEV, Y. D. 2002 Dynamic wetting by liquids of different viscosity. *J. Colloid Interface Sci.* **253** (1), 196–202.
- BONN, D., EGGERS, J., INDEKEU, J., MEUNIER, J. & ROLLEY, É. 2009 Wetting and spreading. *Rev. Mod. Phys.* **81** (2), 739–805.
- CHAN, T. S., KAMAL, C., SNOELJER, J. H., SPRITTLES, J. E. & EGGERS, J. 2020 Cox–voinov theory with slip. *J. Fluid Mech.* **900**, A8.
- CLARKE, A. 1995 The application of particle tracking velocimetry and flow visualisation to curtain coating. *Chem. Eng. Sci.* **50** (15), 2397–2407.
- COX, R. G. 1986 The dynamics of the spreading of liquids on a solid surface. part 1. viscous flow. *J. Fluid Mech.* **168**, 169–194.
- DEVAUCHELLE, O., JOSSERAND, C. & ZALESKI, S. 2007 Forced dewetting on porous media. *J. Fluid Mech.* **574**, 343–364.
- DUSSAN V., E. B. 1976 The moving contact line: The slip boundary condition. *J. Fluid Mech.* **77** (4), 665–684.
- DUSSAN V., E. B. & DAVIS, S. H. 1974 On the motion of a fluid–fluid interface along a solid surface. *J. Fluid Mech.* **65** (1), 71–95.
- EGGERS, J. & EVANS, R. 2004 Comment on “dynamic wetting by liquids of different viscosity”. *J. Colloid Interface Sci.* **280** (2), 537–538.
- FRICKE, M., KÖHNE, M. & BOTHE, D. 2019 A kinematic evolution equation for the dynamic contact angle and some consequences. *Physica D* **394**, 26–43.
- FULLANA, T., ZALESKI, S. & POPINET, S. 2020 Dynamic wetting failure in curtain coating by the volume-of-fluid method: Volume-of-fluid simulations on quadtree meshes. *Eur. Phys. J. Spec. Top.* **229** (10), 1923–1934.
- HOCKING, L. M. 1977 A moving fluid interface. part 2. the removal of the force singularity by a slip flow. *J. Fluid Mech.* **79** (2), 209–229.
- HOCKING, L. M. 1992 Rival contact-angle models and the spreading of drops. *J. Fluid Mech.* **239**, 671–681.
- HUH, C. & SCRIVEN, L. E. 1971 Hydrodynamic model of steady movement of a solid/liquid/fluid contact line. *J. Colloid Interface Sci.* **35**, 85–101.
- JOHANSEN, H. & COLELLA, P. 1998 A cartesian grid embedded boundary method for poisson’s equation on irregular domains. *J. Comput. Phys.* **147**, 60–85.
- KAMAL, C., SPRITTLES, J. E., SNOELJER, J. H. & EGGERS, J. 2019 Dynamic drying transition via free-surface cusps. *J. Fluid Mech.* **858**, 760–786.
- KEELER, J. S., BLAKE, T. D., LOCKERBY, D. A. & SPRITTLES, J. E. 2022 Putting the micro into the macro: A molecularly augmented hydrodynamic model of dynamic wetting applied to flow instabilities during forced dewetting. *J. Fluid Mech.* **953**, A17.
- KISTLER, S. F. 1984 The fluid mechanics of curtain coating and related viscous free-surface flows with contact lines. PhD thesis, ETH Zürich.
- KULKARNI, Y., FULLANA, T. & ZALESKI, S. 2023 Streamfunction solutions for some contact line boundary conditions: Navier slip, super slip and the generalized navier boundary condition. *Proc. R. Soc. A* **479** (2278), 20230141.

- LIU, C.-Y., VANDRE, E., CARVALHO, M. S. & KUMAR, S. 2016 Dynamic wetting failure and hydrodynamic assist in curtain coating. *J. Fluid Mech.* **808**, 290–315.
- LĀČIS, U., JOHANSSON, P., FULLANA, T., HESS, B., AMBERG, G., BAGHERI, S. & ZALESKI, S. 2020 Steady moving contact line of water over a no-slip substrate: Challenges in benchmarking phase-field and volume-of-fluid methods against molecular dynamics simulations. *Eur. Phys. J. Spec. Top.* **229** (10), 1897–1921.
- LĀČIS, U., PELLEGRINO, M., SUNDIN, J., AMBERG, G., ZALESKI, S., HESS, B. & BAGHERI, S. 2022 Nanoscale sheared droplet: Volume-of-fluid, phase-field and no-slip molecular dynamics. *J. Fluid Mech.* **940**, A10.
- MOFFATT, H. K. 1964 Viscous and resistive eddies near a sharp corner. *J. Fluid Mech.* **18** (1), 1–18.
- NAVIER, C. L. M. H. 1823 Mémoire sur les lois du mouvement des fluides. *Mém. Acad. R. Sci. Inst. France* pp. 389–440.
- NGAN, C. G. & DUSSAN V., E. B. 1984 The moving contact line with a 180° advancing contact angle. *Phys. Fluids* **27** (12), 2785–2787.
- POPINET, S. 2003 Gerris: A tree-based adaptive solver for the incompressible Euler equations in complex geometries. *J. Comput. Phys.* **190** (2), 572–600.
- POPINET, S. 2009 An accurate adaptive solver for surface-tension-driven interfacial flows. *J. Comput. Phys.* **228** (16), 5838–5866.
- POPINET, S. 2015 A quadtree-adaptive multigrid solver for the serre–green–naghdi equations. *J. Comput. Phys.* **302**, 336–358.
- POPINET, S. 2018 Numerical models of surface tension. *Annu. Rev. Fluid Mech.* **50**, 49–75.
- QIAN, T., WANG, X.-P. & SHENG, P. 2006 A variational approach to moving contact line hydrodynamics. *J. Fluid Mech.* **564**, 333–360.
- SHIKHMURZAEV, Y. D. 1993 The moving contact line on a smooth solid surface. *Int. J. Multiph. Flow* **19** (4), 589–610.
- SHIKHMURZAEV, Y. D. 2006 Singularities at the moving contact line: Mathematical, physical and computational aspects. *Physica D* **217** (2), 121–133.
- TRYGGVASON, G., SCARDOVELLI, R. & ZALESKI, S. 2011 *Direct Numerical Simulations of Gas–Liquid Multiphase Flows*. Cambridge: Cambridge University Press.
- VANDRE, E., CARVALHO, M. S. & KUMAR, S. 2014 Characteristics of air entrainment during dynamic wetting failure along a planar substrate. *J. Fluid Mech.* **747**, 119–140.
- VARMA, A., ROY, A. & PUTHENVEETIL, B. A. 2021 Inertial effects on the flow near a moving contact line. *J. Fluid Mech.* **924**, A36.
- VOINOV, O. V. 1976 Hydrodynamics of wetting. *Fluid Dyn.* **11** (5), 714–721.
- WEINSTEIN, S. J. & RUSCHAK, K. J. 2004 Coating flows. *Annu. Rev. Fluid Mech.* **36**, 29–53.
- WILSON, M. C. T., SUMMERS, J. L., SHIKHMURZAEV, Y. D., CLARKE, A. & BLAKE, T. D. 2006 Nonlocal hydrodynamic influence on the dynamic contact angle: Slip models versus experiment. *Phys. Rev. E* **73** (4), 041606.
- YOUNG, THOMAS 1805 Iii. an essay on the cohesion of fluids. *Philosophical Transactions of the Royal Society of London* (95), 65–87, arXiv: <https://royalsocietypublishing.org/rstl/article-pdf/doi/10.1098/rstl.1805.0005/1463603/rstl.1805.0005.pdf>.